applied sciences

MDPI

Article

Geoelectrical Characterization of Sedimentary Landslides in the Laguna Del Amor Area, Chota-Cajamarca (Peru)

Arturo Zevallos [1], Julio Torres [2], Cristian Segura [2], Javier Carrasco [1] and Pedro Carrasco [1,*]

[1] Department of Cartographic and Terrain Engineering, Higher Polytechnic School of Ávila, University of Salamanca, Av. Hornos Caleros, n°50, 05003 Ávila, Spain; arturo.zevallos@gmail.com (A.Z.); tgeofisicas@gmail.com (J.C.)

[2] Facultad de Ciencias de la Ingeniería, Escuela Profesional de Ingeniería Civil, Universidad Nacional Autónoma de Chota, Chota 06121, Peru; 2020051032@unach.edu.pe (J.T.); 2019052031@unach.edu.pe (C.S.)

* Correspondence: retep81@usal.es

Abstract: This study focuses on the geometric and geophysical characterization of sedimentary landslides in the Laguna del Amor area, located in Chota-Cajamarca (Peru). The main objective was to identify key static factors related to landslide susceptibility, including slope angle, soil composition, and groundwater flow, prioritizing the areas affected by landslides. Electrical Resistivity Tomography (ERT) was the geophysical method selected because of its effectiveness in delineating subsurface geometries, detecting water content, and assessing mass movements. The methodology combined geophysical analysis (ERT), field geology, and photogrammetry to develop a detailed subsurface model. The results indicate a rotational landslide mainly composed of weathered shales and limestones, with highly saturated zones that increase the area's hazard level. The investigation also identified significant variability in landslide depth throughout the study area, highlighting the importance of these factors in geotechnical risk assessment. This interdisciplinary approach not only contributes to geological knowledge of the area but also provides critical information for mitigation and risk management strategies in landslide-prone areas.

Keywords: electrical resistivity tomography; geoelectrical characterization and subsurface modeling; landslides; shale rocks and calcareous rocks

check for updates

Academic Editor: Nikolaos Koukouzas

Received: 6 January 2025
Revised: 16 February 2025
Accepted: 17 February 2025
Published: 21 February 2025

Citation: Zevallos, A.; Torres, J.; Segura, C.; Carrasco, J.; Carrasco, P. Geoelectrical Characterization of Sedimentary Landslides in the Laguna Del Amor Area, Chota-Cajamarca (Peru). *Appl. Sci.* **2025**, *15*, 2327. https://doi.org/10.3390/app15052327

1. Introduction

Landslides are complex and destructive geological phenomena, common in the mountainous areas of Peru [1,2]. They represent one of the most significant mass movements due to the serious material and human damage they cause, including thousands of deaths and economic losses [3,4]. In response to this problem, several studies have explored the effectiveness of Electrical Resistivity Tomography (ERT) as a non-invasive tool for the investigation and characterization of these geological events; it also detects saturated areas [5–7].

Research in various geographical contexts, such as Italy, Poland, Jordan, Turkey and the Czech Republic, has demonstrated the usefulness of ERT for identifying discontinuities, characterizing landslide geometry, and assessing potential risks [8,9]. In these cases, ERT has been combined with techniques such as digital aerial photogrammetry, providing a deeper understanding of the surface and subsurface structures of the affected areas.

The stratigraphy and materials involved in landslides range from loose sediments to bedrock formations [2]. In this context, ERT, in 2D and pseudo 3D configurations, has proven to be a valuable tool for detecting changes in the subsurface by measuring resistivities, thus making it possible to delineate the geometry of mass movements, detect water content, and evaluate ground motion, fundamental objectives in geotechnical studies [10,11].

The research carried out by [12] sought to analyze the soft rock of the Bengkulu-Lebong North Mountain Road landslide; for them, the data collected from the ERT were processed with Res2Dinv software, thus highlighting it as an effective method for landslide analysis in humid areas (water infiltration). Hence, they conclude that areas potentially subject to subsidence are clayey rocks. Likewise, the aquifer layer makes them susceptible to landslides, in addition to the slopes of 35–55°.

Geophysical methods are presented as a great advantage in the exploration of the subsoil since they allow the collection of data at great depths, with a very high reliability, and they are applicable to a multitude of geological phenomena or terrain characterizations; their application is widely diverse, from engineering to archaeology, always hand in hand with other studies, destructive or non-destructive.

Such is the case of the analysis of slopes treated to cycles of freezing and thawing and earthquakes, these affect the stability of slopes presenting greater structural degradation with respect to the case without freezing and thawing; reducing the affection of the natural frequency environment and increasing the seismic amplification in the slope; and facilitating progressive landslides [13]. These causes highlight the importance of geophysical studies in the evaluation of slope instability.

The enhanced discontinuous deformation analysis (3D DDA) simulation of the slope in Tibet reveals that secondary discontinuities influence the fragmentation and trajectories of blocks, affecting nearby infrastructures [14].

Similarly, the kinematic evolution of rockfalls can be evaluated, with the slope angle having a major impact on block kinematics, followed by the block mass, height of fall, block shape, and angle of fall [15]. This quantitative approach helps to understand the mechanisms of instability and mitigate risks.

In the Shuping landslide, the particle swarm optimization algorithm optimizes landslide prediction by considering the temporal evolution of the slope [16], which in turn would enrich any study as a complementary evaluation of geophysical studies.

The ERT proves to be a relevant geophysical method for predicting ground properties evaluated in the field as the previous geophysical methods, as long as it is accompanied by correlative studies, either destructive or non-destructive.

Anisotropy is particularly relevant for understanding subsurface geology and structure since resistivities vary in value depending on the layers and types of rocks present, such as igneous, sedimentary, and metamorphic [17]. In recent studies, the application of ERT has allowed the identification of important geological faults, as in the Baza fault in Spain, where deep characterizations of up to 1000 m were achieved using the Pole-Dipole array [18]. Similarly, in the Zhangdian-Renhe active fault zone, four fault zones with inclinations between 60° and 75° were identified using ERT [19]. In addition, research on karst cavities has shown that detection is most effective in resistive source rocks, as evidenced in the "Forststraben Einbruch" cavity [20].

In Peru, TRE has been used mainly for road maintenance and groundwater exploration projects [21,22] to characterize the subsoil where these projects were developed, although its application in landslide characterization has been limited. A relevant case is the landslide that occurred on 15 March 2021 in the "Laguna del Amor" area, in Chota, Cajamarca. This event affected 500 m of roadway, houses, local crops, and a riverbank, impacting an area of 16.10 hectares characterized by geomorphologic instability and great tourist importance [23]. The physical–mechanical properties of the slopes of the study area are soils with 22% to 27% moisture and with a granulometry of inorganic clay of high plasticity

(CH). In addition, plastic limits were of 19% and 31% and liquid limits were of 53% and 64% [24].

This paper uses 2D ERT, the most widely used geophysical approximation method, to investigate and represent the electrical properties of the subsurface based on resistivity contrasts, to characterize the distribution of this property in the subsurface [18–26], and to characterize the landslide in Laguna del Amor, with the objective of determining key parameters such as soil composition, saturated strata or water flows, and landslide stratigraphy. This information is crucial for risk management and future urban planning in a region historically affected by recurrent ground movements since 1970.

The research aims to provide detailed knowledge of the sedimentary formations of the area, characterized by high water saturation at significant depths. The landslide in the Lagunas sector was caused by the excessive rainfall in the area and the type of materials characteristic of the geological formations present in the area, and soil originated from the weathering of shale rock (main component of the Chota and Celendín formations); which, together with high saturation, are the triggers of the landslide. The results obtained should be validated by means of geological drilling logs, improving the accuracy and usefulness of the conclusions for further research.

The main challenges encountered in the development of this research are the lack of information on the study area, not presenting information from previous geophysical studies, limiting the comparative analysis, in addition to the difficulties regarding the accessibility of the area, and preventing the constant monitoring of the landslide. The difficulty of the work area, its touristic importance, the methodology (combination of geology, photogrammetry, ERT dipole pole with RES2DINV v. 3.5.3), and the lack of information and resources of the place are part of the challenge present in this research and, therefore, the novelty.

The possible damages generate the need to implement mitigation actions, such as deep drainage to reduce saturation and improve natural drainage, in order to stabilize the water table and partially restore soil cohesion in the most compromised areas.

2. Study Area

The study was conducted at a site located in the Laguna del Amor area, southeast of the city of Chota (Cajamarca, Peru), at an altitude between 2423 and 2622 m.a.s.l. (Figure 1). This area includes a road reconstructed after the landslide occurred in 2021, as well as a set of cracks filled by material dragged due to weathering and erosion processes caused by runoff. These cracks delimit the main fracture of the landslide, in addition to the presence of houses within the danger zone associated with the event, along with several stationary lagoons, including the Laguna del Amor, which gives its name to the area.

For the geophysical evaluation, Electrical Resistivity Tomography (ERT) measurements were used in 2D and pseudo 3D configurations, applied due to the difficulty of the terrain not allowing parallel ERT profiles. Four profiles were designed and analyzed: the first one was plotted along the longitudinal axis of the landslide in the SE–NW direction, following the identified direction of the avalanche movement (Figure 2), while the remaining three were plotted in NE–SW transverse directions to obtain a detailed model of the affected area. For the selection of the field profiles, a photogrammetric survey was carried out in addition to a field reconnaissance in order to identify the areas that would provide the most information for the ERT profiles. The predominant slope in the area varies between 0% and 15% (Figure 2).

In the study area, stationary lagoons, a creek at the foot of the landslide, cracks, inclined trees, geological formations, and geomorphological units of the site can be observed. The landslide in the Laguna del Amor area has an SE–NW direction (Figure 3), whose morphology and orientation suggest an active process due to the presence of tension cracks in the upper crown and at the foot of the landslide slope. In addition, the creek that erodes the foot of the slope Figure 4b,f,h, with jump heights in the escarpment or main landslide crown of between 10 to 15 m, describes a well-defined fault zone. These conditions, together with the topography of the site, helped to define the positioning of the electrodes of the ERT equipment (Figure 3).

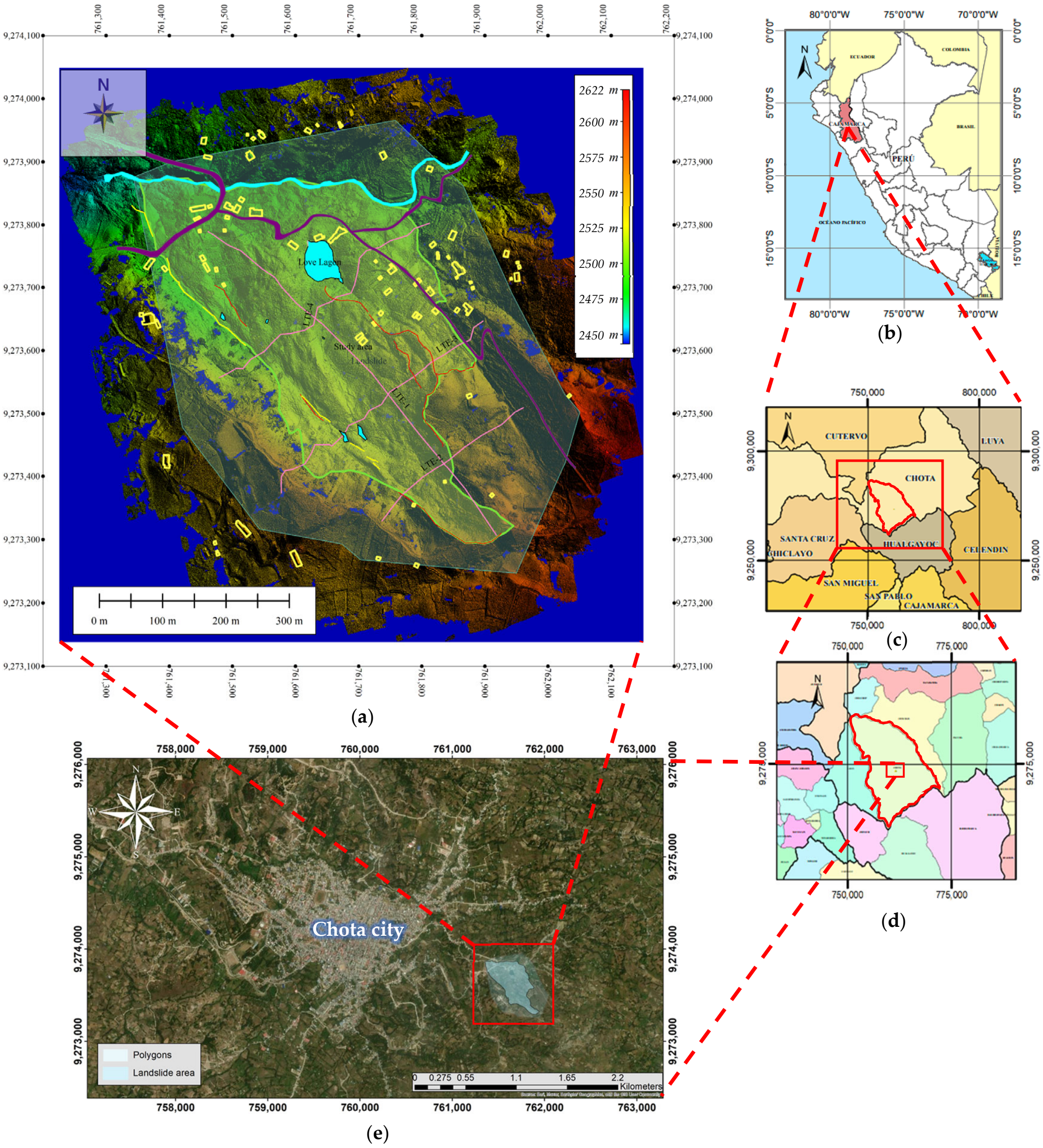

(a) (b) (c) (d) (e)

Figure 1. Location map of the study area. (**a**) Digital height map obtained by DEM photogrammetry of the Laguna del Amor area. Visualizing light blue water bodies, red lines as escarpments or landslide crowns, purple lines as access roads, yellow lines as stress cracks, and yellow polygons as houses built in the study area. (**b**) Location map of Cajamarca in Peru. (**c**) Location map of Chota district in Chota province/(**d**) City of Chota located in the district of Chota, (**e**) Study area located near the city of Chota.

The cracks located in the crown and foot of the landslide present considerable openings, indicating the instability of the terrain, being the consequence of accumulated tensional forces, generating differential displacements in the material (Figure 5) and allowing the infiltration of water, in turn increasing the weight and the hydrostatic pressure in the interior of the sliding mass. The stationary lagoons found near the intersection of ERT 3 and ERT 1 of the lagoon can only occur if there is a clay formation that impedes the flow of water into the terrain, a process that should occur naturally, considering the irregularities of the terrain; the presence of the Laguna del Amor is explained by the existence of a horizontal water table that supplies the lagoon throughout the year, implying that there is a continuous flow of water near the lagoon; the formations present (d and e) located (300 m) northwest and southwest of the Laguna del Amor explain the presence of these materials and the slide, since these are made up of clayey-loamy materials and limestone rocks, which are soluble in water. The presence of these morphological elements suggests that the landslide has advancing kinematics and could undergo acceleration under adverse precipitation or seismic conditions. The gully is at the foot of the landslide and serves to undermine the accumulated material.

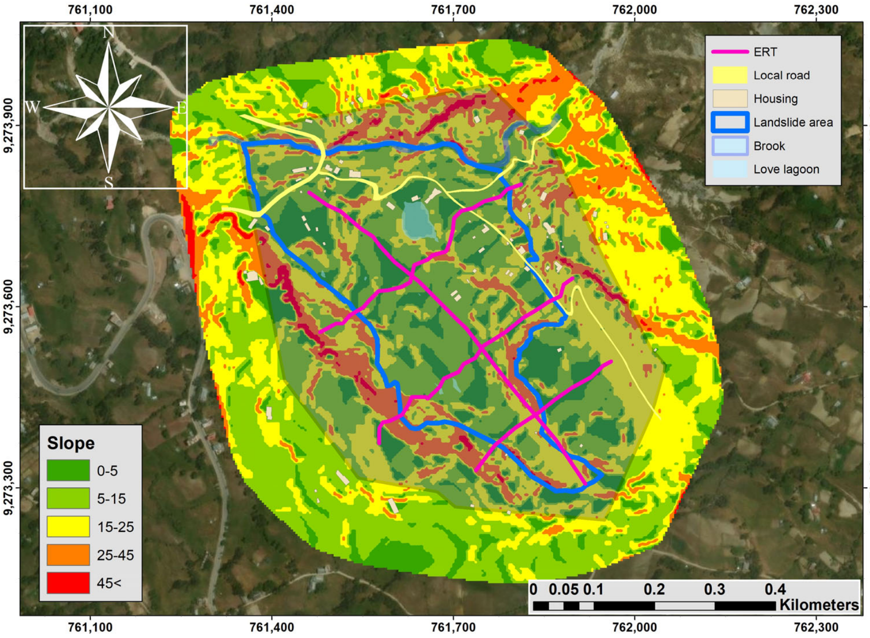

Figure 2. Slope map of the Laguna del Amor landslide.

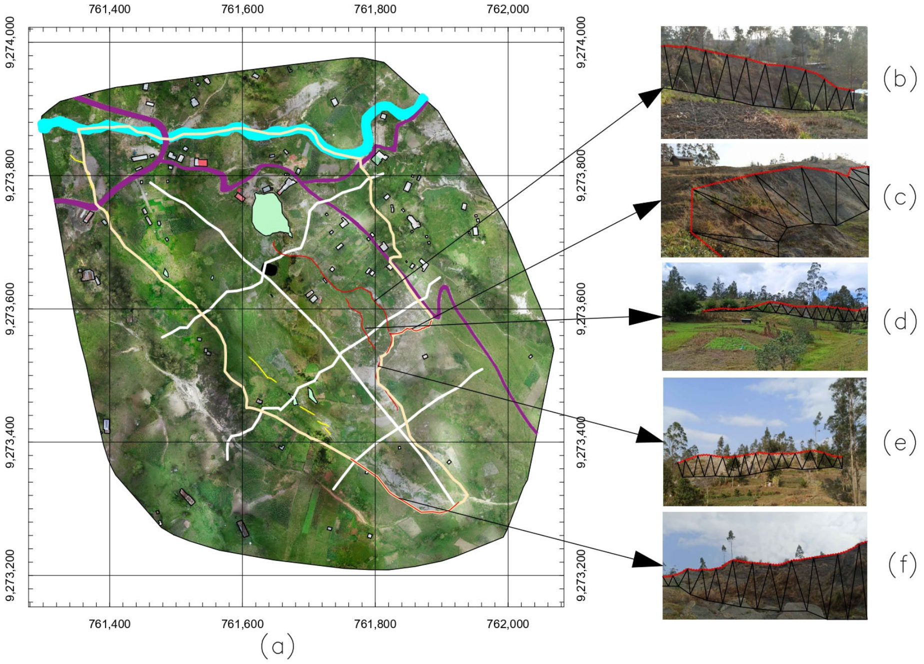

Figure 3. Distribution of escarpments in the Lagunas sector. (**a**) Study area. (**b**) Escarpment 1. (**c**) Escarpment 2. (**d**) Escarpment 3. (**e**) Escarpment 4. (**f**) Escarpment 5.

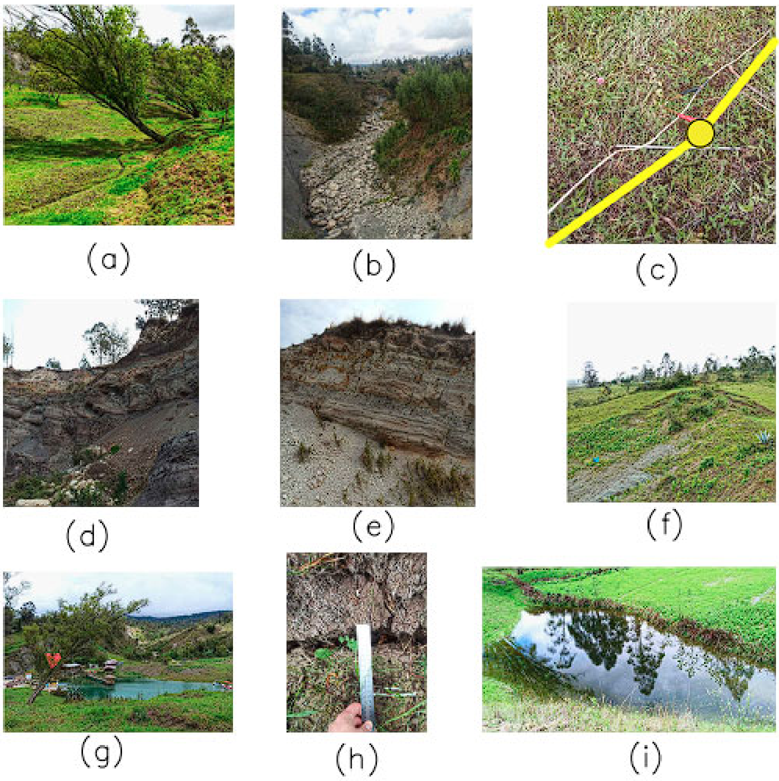

Figure 4. Components of the Lagunas sector. (**a**) Tree inclined by the loss of anchorage in bofedal soil. (**b**) Dry brook. (**c**) Electrical Resistivity Tomography line. (**d**) Structural hill sub-unit in sedimentary rock. (**e**) Limestone rock. (**f**) Landslide crown. (**g**) Laguna del Amor (touristic resource). (**h**) cracks. (**i**) Stationary lagoons during rainfall periods.

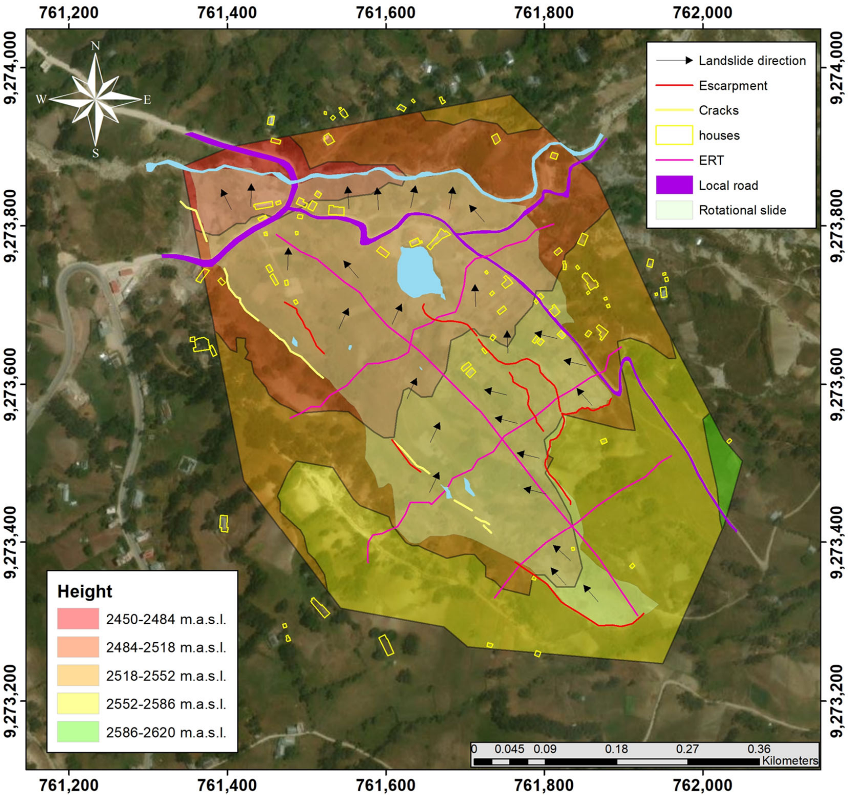

Figure 5. Study area is classified in heights next to arrows with the avalanche line in the Laguna del Amor area.

The landslide event has caused the fall of large trees, such as Salix humboldtiana (Figure 4g), whose loss of anchorage in the soil indicates a considerable alteration of the apparent cohesion and stability of slopes [27,28]. In addition, significant cracking and the collapse of buildings in the affected area have been observed due to the movement of masses at a depth that has displaced the structures and compromised their structural integrity. This phenomenon has also had a negative impact on cultivated areas, where the displacement of the terrain has modified the soil profile, affecting both fertility and the availability of arable land.

2.1. Precipitation Analysis

The maximum precipitation between 2020 and 2024 of the Chota meteorological station (Table 1) was analyzed in millimeters (mm). It is a key factor for the occurrence of landslides, being notable in the phenomenon of 15 March 2021. In addition, the Figure 6 identifies the maximum extent of precipitation in the months of March and April, which is the main factor for landslides in the province of Chota and also in the study area. The months of less precipitation are July, August, and September.

Table 1. Chota weather station data.

Station: Chota					
Department:	Cajamarca	Province:	Chota	District:	Chota
Latitude:	6°32′49.66″	Longitude:	78°38′55.07″	Altitude:	2468 masl.
Type:	CO-Meteorological	Code:	106034		

2.2. Local Geology and Geomorphology

According to the map extracted from the Geological and Mining Cadastral Information System (GEOCADMIN), the geology present in the Laguna del Amor area is within the lower Chota formation (Figure 7). In addition, the province of Chota, located in the 17S Universal Transverse Mercator World Geodetic System (UTM WGS 84), in southern Peru, and in the center of the Cajamarca region, presents a complex geology due to its location near the convergent margin between the South American and Nazca plates [29].

The geomorphological development of the 14f quadrangle of Chota is the result of degradational processes, presenting great unevenness; the structural geology is composed of very diverse phases, sectioning in the tectonic province of Cutervo, tectonic province of Chimú, tectonic province of Pacasmayo, and tectonic province of Santa Cruz. These, in their internal movement, modify the younger formations, folding them, rotating them, and faulting them. The lithostratigraphy of the 14f quadrangle is composed of units originated in the Mesozoic: Pulluicana group (Ks-pu), Quilquiñan group (ks-qui), Cajamarca formation (Ks-ca), and Celendín formation (Ks-ce); in the Cenozoic, there is only the Chota formation, with its three representative members: lower member (Pe-cho/i), middle member (Pe-cho/m), and upper member (Pe-cho/s) [30]. Among all these formations, the Celendín formation and the lower Chota formation stand out since they outcrop in greater proportion in the landslide study area of the Laguna del Amor zone (Figure 8). The geodynamic processes responsible for this high geological complexity are generally external geodynamic processes, including high fluvial precipitation, strong earthquakes, weathering, and the accumulation of large soil masses. On the other hand, anthropic processes can be summarized as follows: the destruction of the vegetation cover (Figure 4a,f,g), evidenced by the inclination of the trees, and the disturbance of the natural slope of the terrain (Figure 4d), which clearly exposes the Chota Formation.

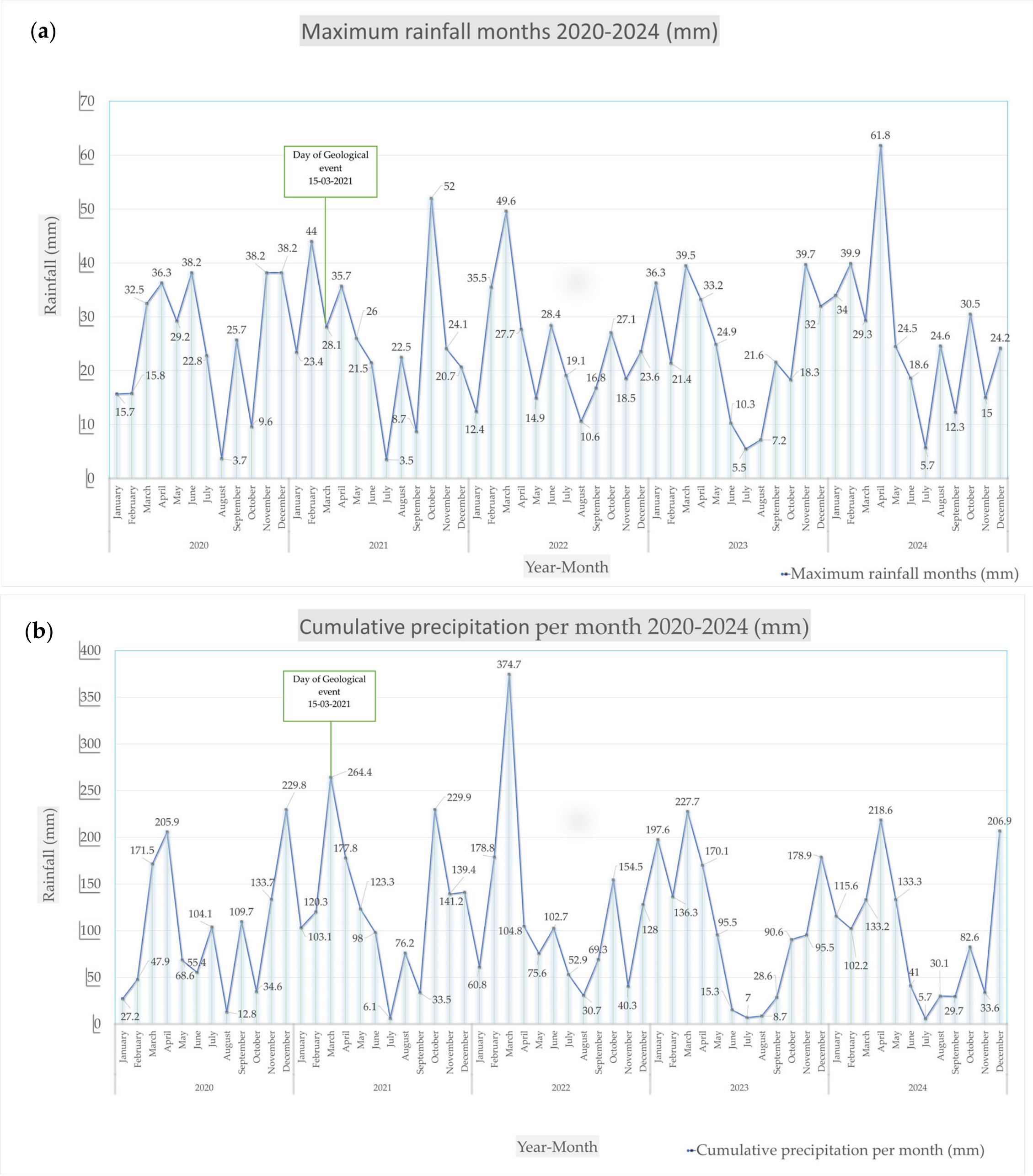

Figure 6. (**a**) Maximum monthly precipitation from 2020–2024. (**b**) Cumulative precipitation per month, 2020–2024 (mm), source: Chota meteorological station, [31].

2.2.1. Chota Formation

In the lithological environment, conglomerates of rounded clasts are observed, mainly of quartzite, sandstone, and a few volcanic rocks, with an average size of 10 cm in a sandy–silty matrix [23–31]. It is characterized by its red hue that changes vertically toward purple. Two clearly delimited parts can be identified: the basal part, formed by clayey sediments such as mudstones, siltstones, and red and yellowish layers, with intercalations of fine-grained gray-greenish sandstones. The shales and mudstones are located in very thick strata with some types of quartz material that rise toward the top in some of the layers. In addition, they symbolize the Cenozoic–Paleozoic system [32].

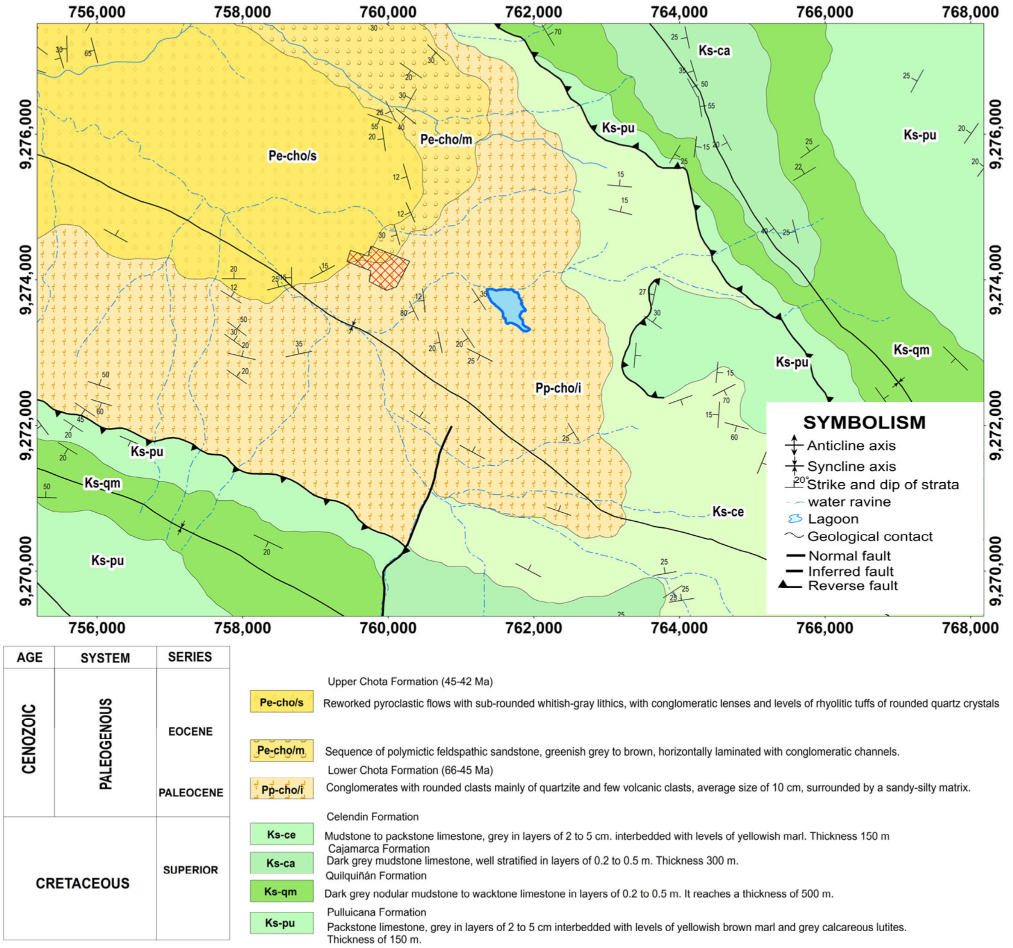

Figure 7. Geology of quadrangle 14f extracted from the database of the Instituto Geológico Minero y Metalúrgico (INGEMMET), stored in the Sistema de Información Geológico y Catastral Minero (GEOCADMIN).

2.2.2. Celendín Formation

The Celendín formation is mainly composed of marl and shale of bluish-gray and reddish-yellow hues that are interspersed with marly limestone and some sandy limestone in its upper part. Additionally, it is possible to identify thin layers of sheets of secondary gypsum dispersed in the clayey material, creating crusts in the calcareous strata. The Celendín formation overlies the Cajamarca formation located below it, which indicates that sedimentation was constant during the period in which both formations were deposited. However, the underlying contract with the Chota formation cannot be determined due to the existence of recent material covering this region. The Celendín formation is considered to symbolize the end of Cretaceous marine sedimentation and the beginning of Cretaceous marine sedimentation [23–32].

The sandy–silty matrix is permeable and facilitates the infiltration of runoff water, which constitutes primary conditions and factors in susceptibility to mass movements (landslides). These rocks are not competent and are easily eroded. Toward the south and east of the evaluated sector, we find an intercalation of shales, marls, and thin limestones of a light yellowish or cream color, which is very fractured, moderately weathered, and quite fossiliferous [23–31]. The intercalation of these materials is susceptible to collapse since the intercalations of shale, due to their behavior when saturated with water, are easily displaced.

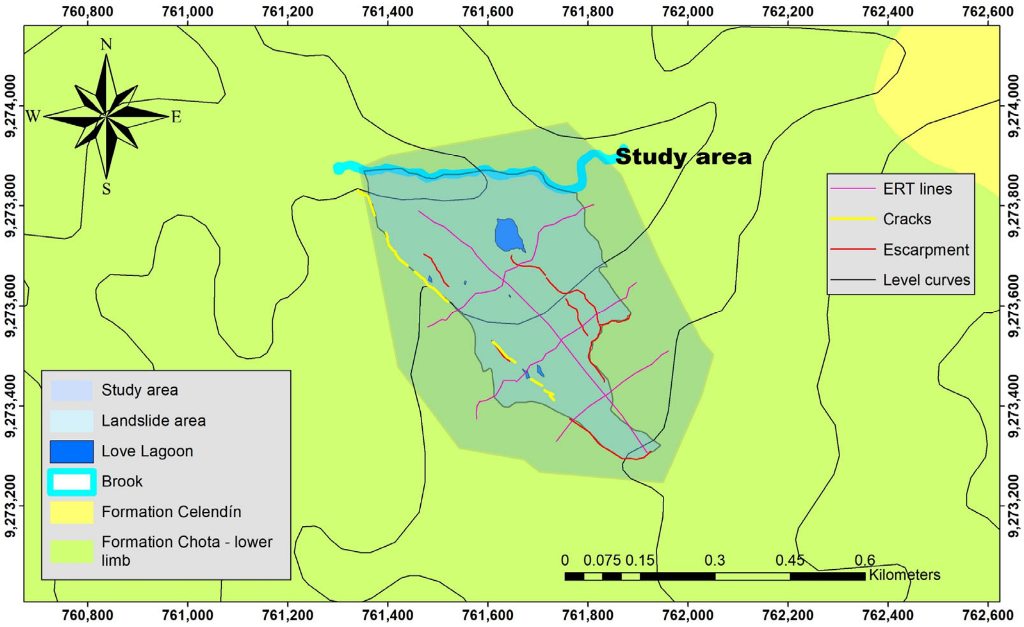

Figure 8. Geological map 1:7000 of the study area extracted from the database [33,34].

2.2.3. Colluvial–Deluvial Slope

Composed of the intercalated accumulation of materials of colluvial and deluvial origin (Figure 9), which are materials of minimal transportation, these deposits are interstratified, without a clear distinction between them [1]. The material in situ is made up of clasts of fossiliferous limestone and yellowish-brown marl, with shapes varying between rounded, sub-rounded, and angular, arranged in different sizes; on the other hand, there is a presence of silt and sand [23–32].

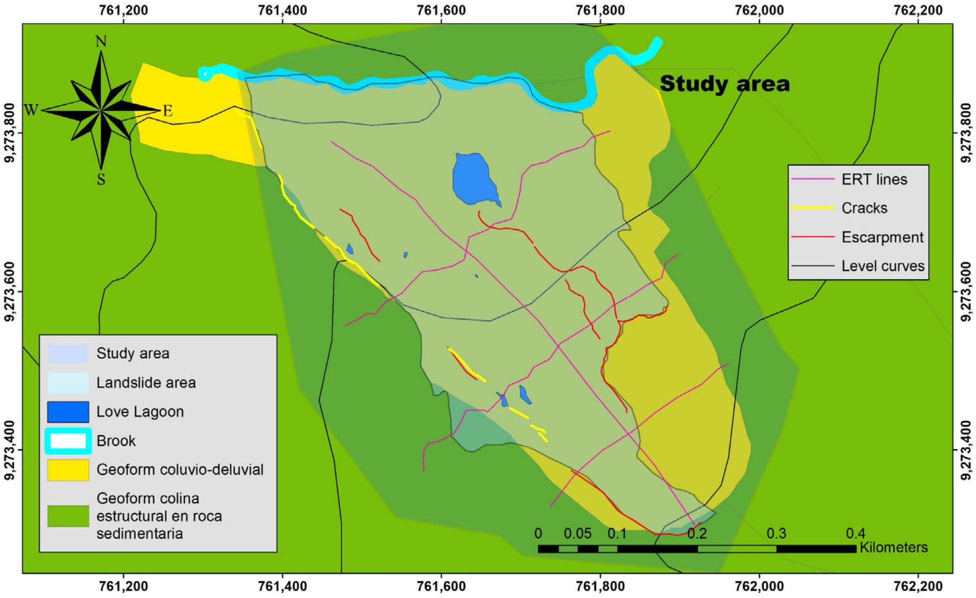

Figure 9. Geomorphological map 1:4500 of the study area extracted from the database of the Geological, Mining, and Metallurgical Institute (INGEMMET), stored in the geological and mining cadastral system (GEOCATMIN).

2.2.4. Structural Hill Subunit in Sedimentary Rock

It is made up of calcareous rocks interbedded with lutites; the geoform is linked to the outcrops of the Celendín Formation [23].

The geology of the Laguna del Amor (Figure 8) landslide is predominantly sedimentary and clayey, consisting of mudstone, siltstone, and marl; in turn, there are also clasts of quartz material marly limestone that is somewhat nodular in thin layers, some with a lamellar texture; with regard to yellowish-gray sandy limestone and nodular limestone with brown and yellowish marl, there are also banks of light limestone with intercalations of sandy shale and thin marl, characteristic of the geological formations of the area. According to [35,36], the presence of sandstone alternating with shale generates a greater probability of mass movements. The presence of shale, mudstone, and weathered marl rocks, ranging in color from gray to reddish-yellow, is interspersed with the presence of clasts and limestone rocks, which in turn are present in multiple landslides [37–39].

3. Electrical Resistivity Tomography for Landslide Assessment

The Electrical Resistivity Tomography (ERT) method is based on measuring the differences in electrical potential along a connected electrode array. By injecting current into the ground using two electrodes (metal stakes), the voltage difference in the subsurface is measured based on Ohm's Law, which provides us with indirect information on water saturation, fluid conductivity, porosity, and surface conductivity. The conductivity of the fluid, the porosity, and the surface conductivity, the latter depending on the organic matter and the clays [18–41], as well as the resistance of the soil strata, can be calculated as follows:

$$R = U/I, \tag{1}$$

where U is the measured voltage and I is the injected current. To obtain accurate ERT results, multiple electrodes are used to minimize measurement errors through proper data inversion [42,43]. Based on the injected current, measured voltage, and electrode configuration (Table 2), a resistivity image or pseudo-section of the subsurface is generated [44].

Table 2. Input data for processing.

Electrodes	24
Interdistence (m)	15–20–30 *
Delay from rising edge (s)	0.02
Acquisition period (s)	0.3
Signal Inversion Delay (s)	0.02
V (mVolts)	5000
I (mA)	1500
Array	Polo-Dipolo
Data Noise Tolerance (%)	2
Number repeat	1
Sample frequency	32,000 Hz
Máximum n	22

* Inter-electrode distances used in ERT, 30 m for ERT-1, 15 m for ERT-2, and 120 m for ERT-3 and ERT-4.

The pole–dipole (Figure 10) array will be used due to its great utility for its good vertical and horizontal resolution, deep penetration, and sensitivity to both vertical and horizontal structures, according to studies by [45,46]. This method is perfect for detecting discontinuities between layers of rock and sediment in geological cross-sections of unstable terrain and also allows for the precise definition of the surface along which the breakage and displacement of the sliding mass occurred. The use of two-dimensional inversion methods is very common in landslide analysis [47], thanks to their resolution, precision, and accuracy, which make it possible to avoid erroneous data [7–37].

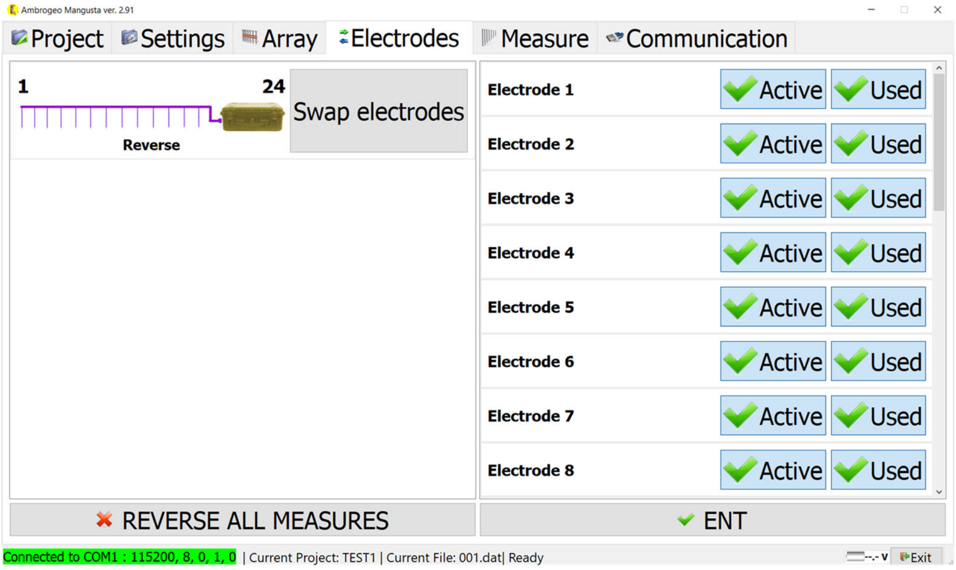

Connected to COM1 : 115200, 8, 0, 1, 0 | Current Project: TEST1 | Current File: 001.dat| Ready

Figure 10. Number, order, activity, and use of electrodes in the arrangement used.

To classify the materials according to their resistivities (Figure 11), the resistivity values of rocks and minerals developed by Orellana [48] will be considered.

Applying 3D ERT monitoring would increase the robustness of the study, as the results show that this method has the lowest false negative rate (2.412%) and the highest detection accuracy (up to 100%), surpassing traditional methods [49]. Similarly, the application of seismic methods, such as seismic refraction, multichannel analysis of surface waves (MASW-MASW-2D), multichannel analysis of microtremors (MAM or REMI), and time domain electromagnetic methods (TDEM), would expand the research to determine compatibility in the different strata and the conductivity of the materials in the study area; however, these methods would lack depth (seismic methods) and electromagnetic methods would be difficult to access.

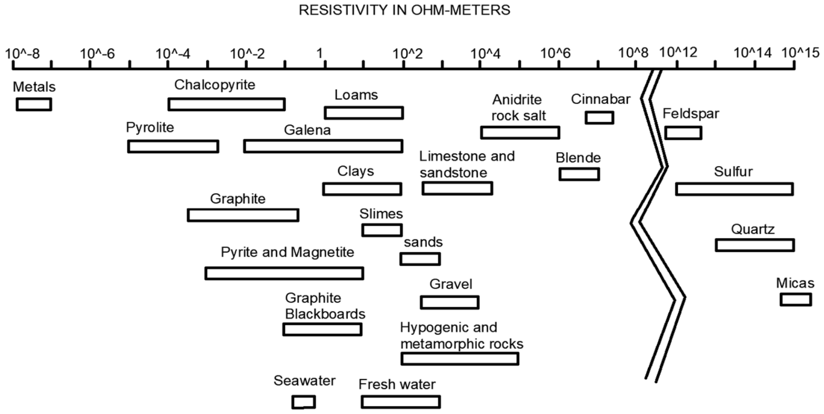

Figure 11. Resistivity values of rocks and minerals.

3.1. Pole–Dipole

The pole–dipole configuration is a technique widely used in electrical tomography to investigate landslides, using one current electrode and two potential electrodes to measure the resistivity of the subsoil. This technique stands out for its good vertical and horizontal resolution, deep penetration, and sensitivity to both vertical and horizontal structures, according to studies by [45–51].

In the field of landslides, the pole–dipole method has proven effective in identifying the sliding surface, detecting areas with water saturation, and distinguishing between stable and unstable materials, as evidenced by the research of [3–53], yet it has not been diversified in this field.

Two-dimensional electrical tomography has great advantages, allowing for high horizontal and vertical resolution, especially with the pole–dipole arrangement, great depth, and flexibility in the field.

ERT was chosen due to the pole–dipole configuration, which provides high sensitivity both horizontally and vertically, enabling the identification of anomalies. This configuration was selected for the following advantages:

○ High resolution in depth and length;
○ It allows the identification and/or contrasting of different geological contacts;
○ It allows the correlation of resistivity values with highly saturated materials;
○ It allows the obtainment of profiles with the topography of the terrain.

3.2. Data Inversion

The data were processed with the inversion program RES2DINV v3.53 from Geotomo Software; this inversion program presents good results in data processing [39]. The inversion routine used by the RES2DINV v3.53 program to obtain the 2D electrical resistivity images of the subsoil is based on the inversion algorithm of the smoothness-constrained least squares method. [54,55]. The two-dimensional model used in this program divides the subsoil into a series of rectangular blocks [56]. This method is also known as the "Block inversion method"; it is efficient in cases of soil resistivities with large contrasts [57]. The resistivity of the blocks is adjusted iteratively to minimize the difference between the measured and calculated apparent resistivity values. The latter are calculated using the finite difference method [58].

The methodology of the RES2DINV ver. 3.53 program uses the following formula based on least squares. An advantage of this method is that the damping factor and the smoothness filters can be adjusted to adapt to different types of data [12–45].

$$\left(J^{T}J + uF\right)d = J^{T}g \tag{2}$$

Donde: $F = f_X f_X^T + f_Z f_Z^T$; f_Z = vertical flatness filter; f_X = horizontal flatness filter; u = damping factor; d = model perturbation vector; g = discrepancy vector; and J = matrix of partial derivatives.

4. Data Collection and Retrieval

4.1. Electrical Resistivity Tomography

The Electrical Resistivity Tomography data began by choosing the profiles, directly correlated with the profiles developed in the risk assessment study by León and Zavaleta [23], taking these profiles as the starting point for the selection of ERT lines, and adding one more ERT profile, in order to cover the greatest number of height intervals (Figure 5). The selection of profiles was changed according to the topography encountered in the field.

Four Electrical Resistivity Tomography sections (ERT-1, ERT-2, ERT-3, and ERT-4) were obtained with measurements in a single direction using the Mangusta System MC 96E device (Figure 12), with an electrode spacing of 30 m for the first section (ERT-1) with a length of 690 m and 15 m and for the second (ERT-2) with a length of 345 m, in addition to 20 m for the third and fourth sections (ERT-3 and ERT-4), both with a length of 460 m.

This allows for a maximum depth of 275 m, 140 m, 175 m, and 190 m, likewise with 22 levels in each line. Once the data were obtained, the RES2DINV v3.53 program was used to obtain the profiles. ERT-1 is the representative section of the main axis of the landslide and is the longest compared to ERT-2, ERT-3, and ERT-4. The lines have been arranged with the aim of covering and evaluating the main axis of the landslide and the low, medium, and high levels of the landslide.

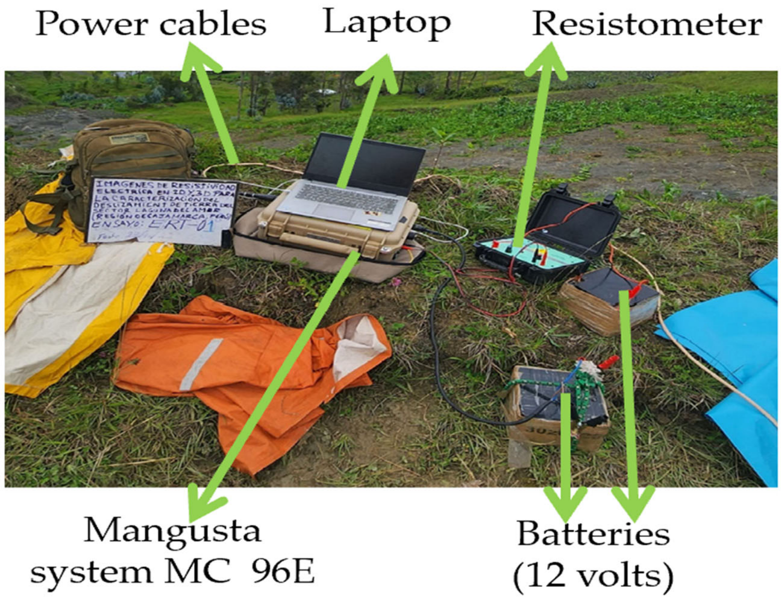

Figure 12. Field image of the MANGUSTA SYSTEM MC96E. Team on the crest of the ERT 1 slope.

4.2. Photogrammetric Survey

Photogrammetric methods are used, as are vertical electrical tomography, to evaluate landslides, which are considered relatively new [59]. The Digital Elevation Model (DEM) method is used to highlight morphological changes in the surface and deep-seated movements [60]. The topographic analysis was carried out by flying over the study area at an altitude of 100 m (Figure 13), following the uniformity of the terrain; with a DJI Phantom 4 Pro drone, which is equipped with a camera with a 1″ sensor and an effective resolution of 20 MP (megapixels), attached to a 3-axis gimbal, which guarantees stability in the shots. Two Class 10 microSD memory cards were used for the drone, featuring transfer speeds of up to 100 MB/s and storage capacities of 16 GB and 32 GB.

The data were processed in the Agisoft Metashape program. This connected the (2D) images through stereoscopy to generate a 3D model of the study area. n Agisoft Metashape, the densified point cloud to be classified, with points associated with buildings, vegetation, and human-made objects partially, must be removed. Global Mapper software v26.0 is used to create Digital Surface Models (DSMs), export point clouds, retrieve elevation values, classify point clouds, and export files in various formats.

Agisoft Metashape will be used for point cloud management, primarily to remove unwanted points. It is an essential step for transferring the densified point cloud to Autodesk Civil 3D and ArcMap 10.8 [61].

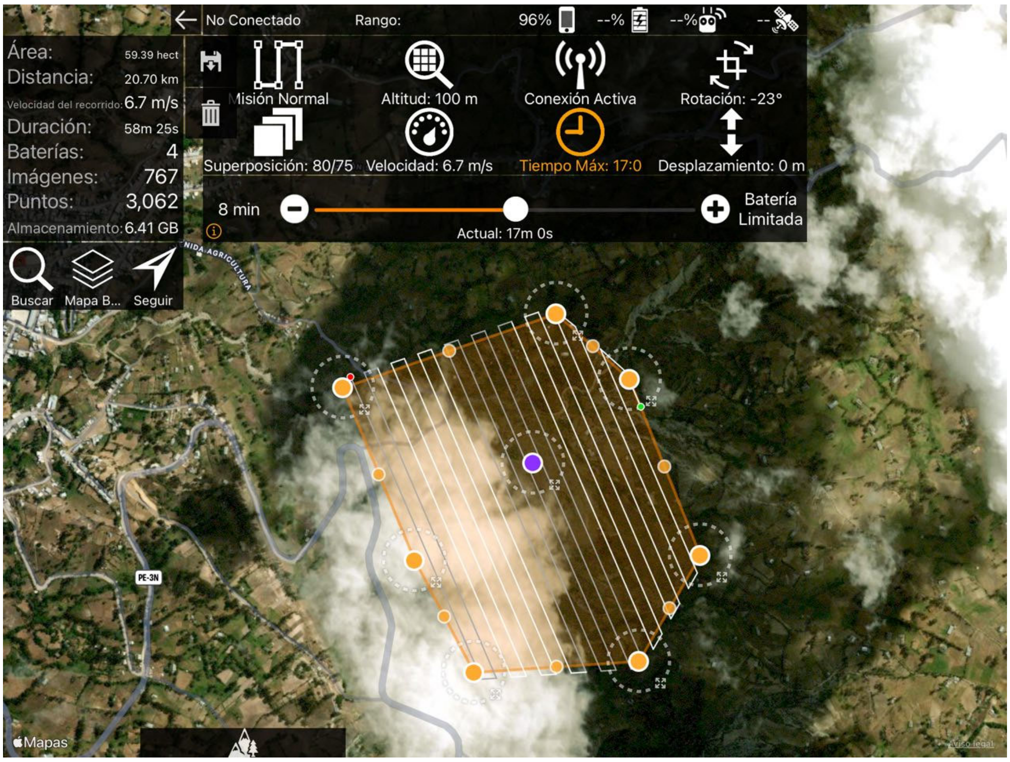

No Conectado
Rango:
96%
--%
--%
--
Área: 59.39 hect
Distancia: 20.70 km
Velocidad del recorrido: 6.7 m/s
Duración: 58m 25s
Baterías: 4
Imágenes: 767
Puntos: 3,062
Almacenamiento: 6.41 GB
Misión Normal
Altitud: 100 m
Conexión Activa
Rotación: -23°
Superposición: 80/75
Velocidad: 6.7 m/s
Tiempo Máx: 17:0
Desplazamiento: 0 m
8 min
Batería Limitada
Actual: 17m 0s

Figure 13. Flight plan for the photogrammetric survey.

5. Results

The line called ERT-1, with a SE–NW direction, intersects with the second ERT at 150 m, with the third ERT at 307. 5 m and the fourth ERT at 471.75 m, coinciding with the delimitation of the beginning of the zone of maximum humidity; the old fault plane of the landslide of the year 2021 is identified along the zone that appears to have the greatest water flow, and this is represented by a yellow line while the black line represents the possible extension of the landslide. The stratigraphy observed in the profile exhibits consistent horizontality, becoming irregular from 450 m to the end of the line. In this section, the upper stratum (Stratum 1), with resistivities ranging from 0.6 to 8.8 Ohm·m, presents discontinuities. Stratum 2, with resistivities between 8.8 and 92.3 Ohm·m, shows an increase in thickness, while the lower stratum (92.3 to 666 Ohm·m) reaches its lateral extension limit (Figure 14a). Stratum 1 has a thickness ranging from 25 to 75 m and consists of calcareous materials interspersed with shales, as well as rounded, sub-rounded, and angular clasts with high saturation levels; stratum 2, with depths of between 35 and 55 m thick, are attributed to a material consisting of a slightly moist sedimentary rock of the limestone type with intercalated shale; and Stratum 3, of unknown thickness, consists of slightly moist limestone interbedded with shale (Figure 14b). The stratigraphic predominance of low resistivity materials, which allude to saturated clayey materials, at shallow depths increases the susceptibility to mass landslides attributed to the high saturation of its materials.

In the length of the ERT-2 (Figure 15a), with the NE–SW direction, it is possible to distinguish a first part composed of the structural hill subunit in sedimentary rock from 21.6 m to 135 m; from 135 m there is contact between the colluvio-deluvial geomorphological subunits and the structural hill in sedimentary rock up to 165 m, and at 165 m, the landslide begins and extends up to 292.8 m (Figure 15b). There are strata of high saturation at low depth represented by the blue colored stratum where the rupture plane of the landslide develops, denoted by a red line, which extends between 44 m and 13 m deep in the profile. It intersects with ERT-1 at progressive 202.2 m and with landslide scarp 1 at progressive 160 m. Stratum 1, characterized by low resistivity and represented by bluish colors, exhibits inconsistent horizontality throughout the profile. Stratum 2 maintains consistent horizontality with a slight dip up to progressive 240 m, where it increases in thickness. Stratum 3 is scarcely present in the profile, extending up to progressive 233 m, where it disappears completely (Figure 15a). The lack of continuity and horizontality in the strata shows a recent earth movement in the first layer of the landslide. The composition of the strata present in this profile is the same as in ERT-1, belonging to the same geology and geomorphology.

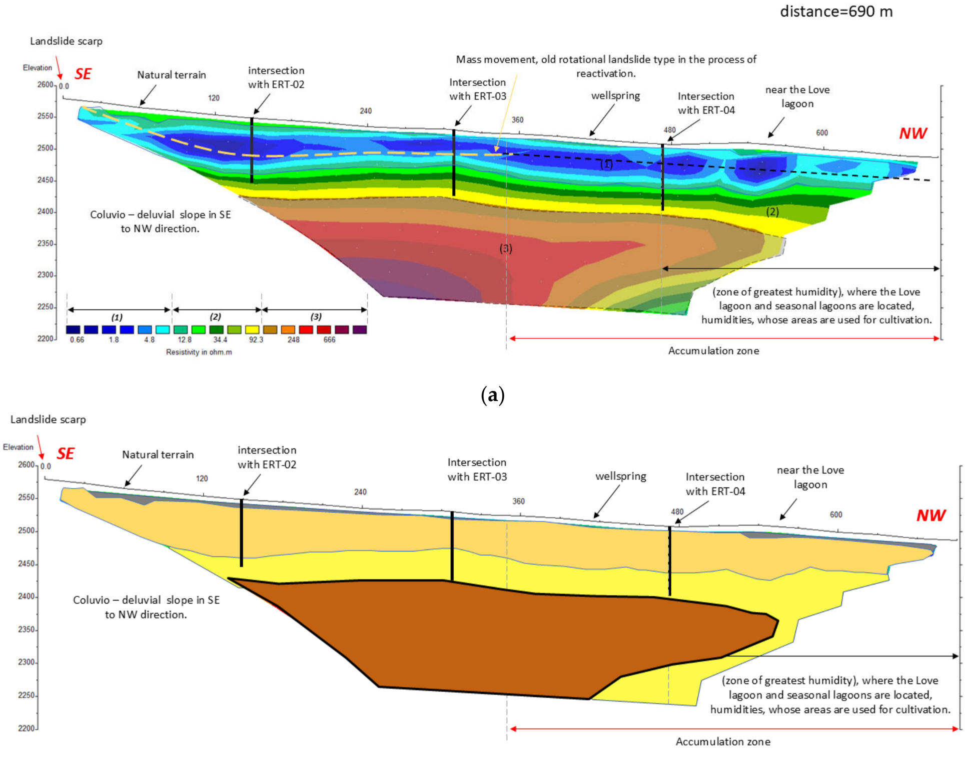

(a)

(b)

Figure 14. ERT 1 profile. (**a**) Profile interpreted with respect to the resistivities obtained in the field readings. (**b**) Stratigraphic profile.

The ERT-3 profile, oriented in an SE–NW direction, shows an intercalation of structural hill subunits in sedimentary rock and Colluvial–Deluvial slope from the beginning of the line up to 207 m. A local road intersects the profile at 43 m, while the landslide begins at 47 m and extends to 380 m. At 111 m, the profile approaches scarp 1, and at 219 m, it intersects with ERT-1. At 333 m, stationary ponds, typically present from February to March, are observed (Figure 16a). This section also contains rounded quartzite and sandstone clasts embedded in a sandy–silty matrix; in turn, it is possible to appreciate greater saturation in stratum 1 (presence of wetlands Figure 3a,g) which, like profile ERT-1, shows inconsistent horizontality caused by an ground movement, in addition to the continuation of a possible slip fault plane, information difficult to confirm due to the high saturation of stratum 1; stratum 2 also shows little horizontality in addition to an overlap of strata between 1 and 2, which suggests that the landslide begins to accumulate its mass from this profile; and stratum 3 has a complete presence in this stratum, in addition to presenting good horizontality, so it is understood that this stratum is not affected by the landslide Figure 16b). The composition of the landslide is consistent with that observed in ERT-1 and ERT-2.

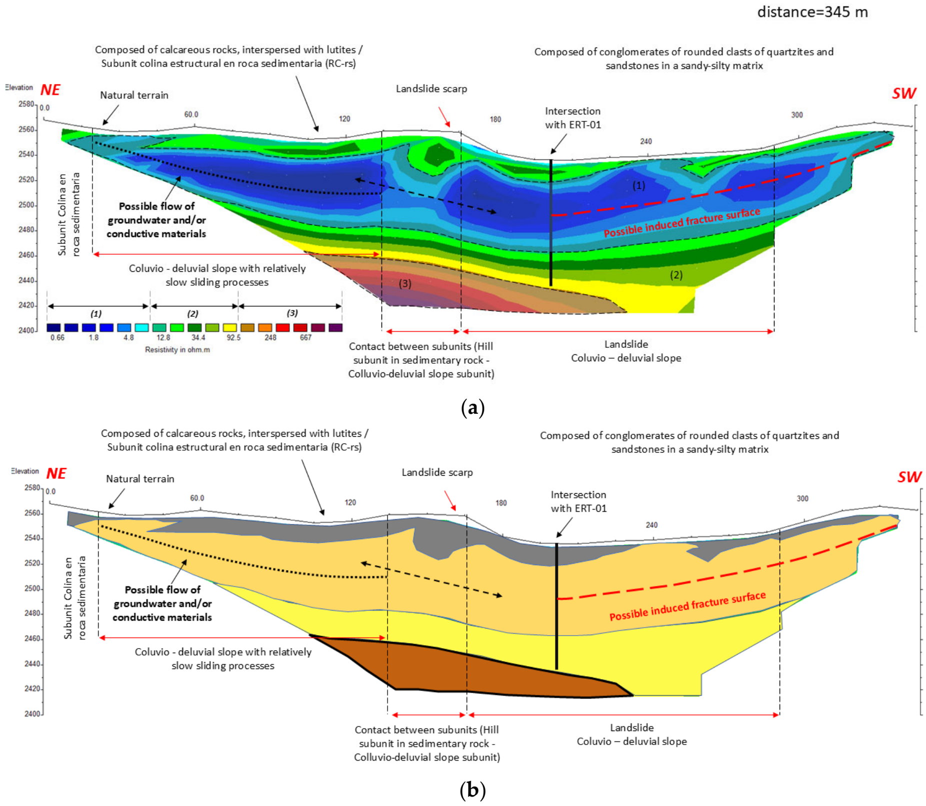

Figure 15. ERT-2 profile. (**a**) Profile interpreted with respect to the resistivities obtained in the field readings. (**b**) Stratigraphic profile.

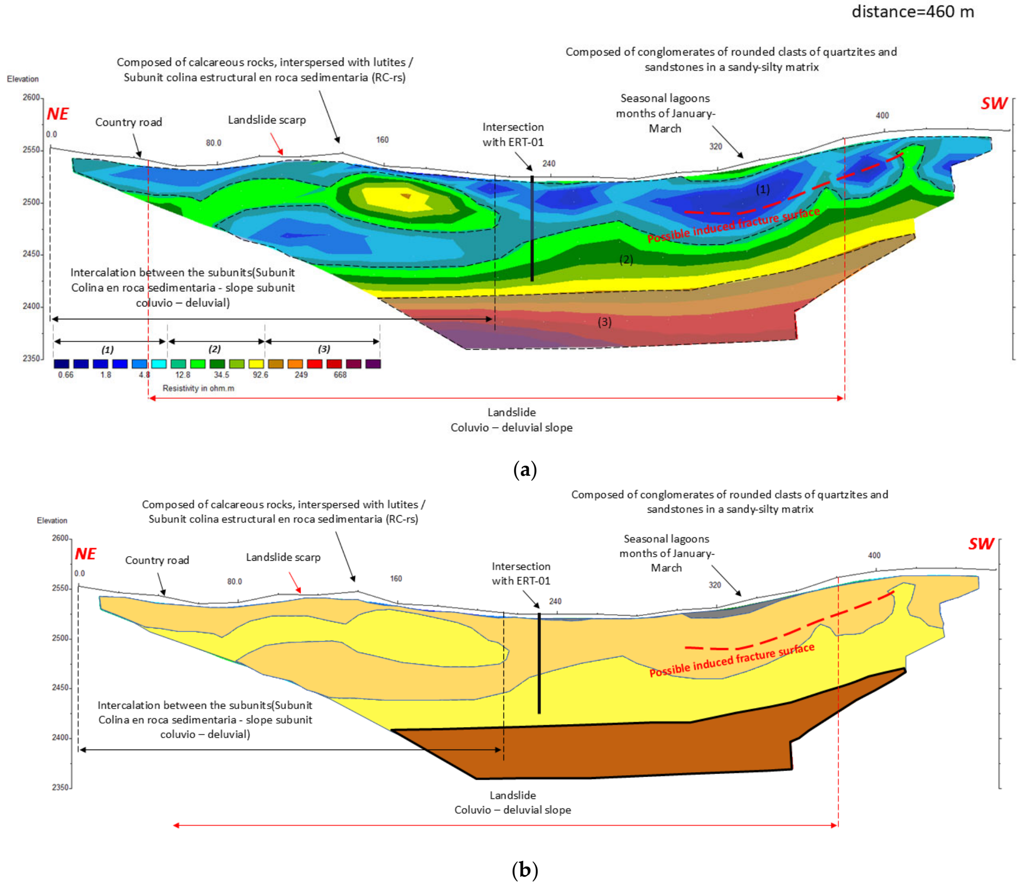

Figure 16. ERT-3 profile. (**a**) Interpreted profile with respect to the resistivities obtained in the field readings. (**b**) Stratigraphic profile.

In the ERT-4 profile, with an SE–NW direction, the landslide begins at 25.9 m and extends to 390 m, at 272. Overall, 8 m is the intersection with profile ERT-1, as is the case with profile ERT-3; at 120 m it is possible to note an intercalation of subunits: a structural hill in sedimentary rock and a Colluvial–Deluvial slope is present, in addition to a composition of rounded quartzite and sandstone clasts in a sandy–silty matrix from 320 m to the end of the profile, and the presence of the lagoon near the profile is explained by the presence of a zone of maximum humidity. From the beginning of the profile to 381 m, this, in turn, generates a water table of strange dimensions parallel to the brook; layer 1 presents an inconsistent horizontality, and furthermore, like the ERT-3 profile, it presents a possible fault plane that cannot be predicted due to the saturation of layer 1. Layer 2 maintains consistent horizontality up to a progressive 345 m, where it increases in thickness (Figure 17a). Similar to the ERT-3 profile, this layer overlaps layers 1 and 2 due to the profile's location in the landslide's mass accumulation area. Layer 3 is scarcely present in the profile and disappears completely at the 360-m mark (Figure 17b).

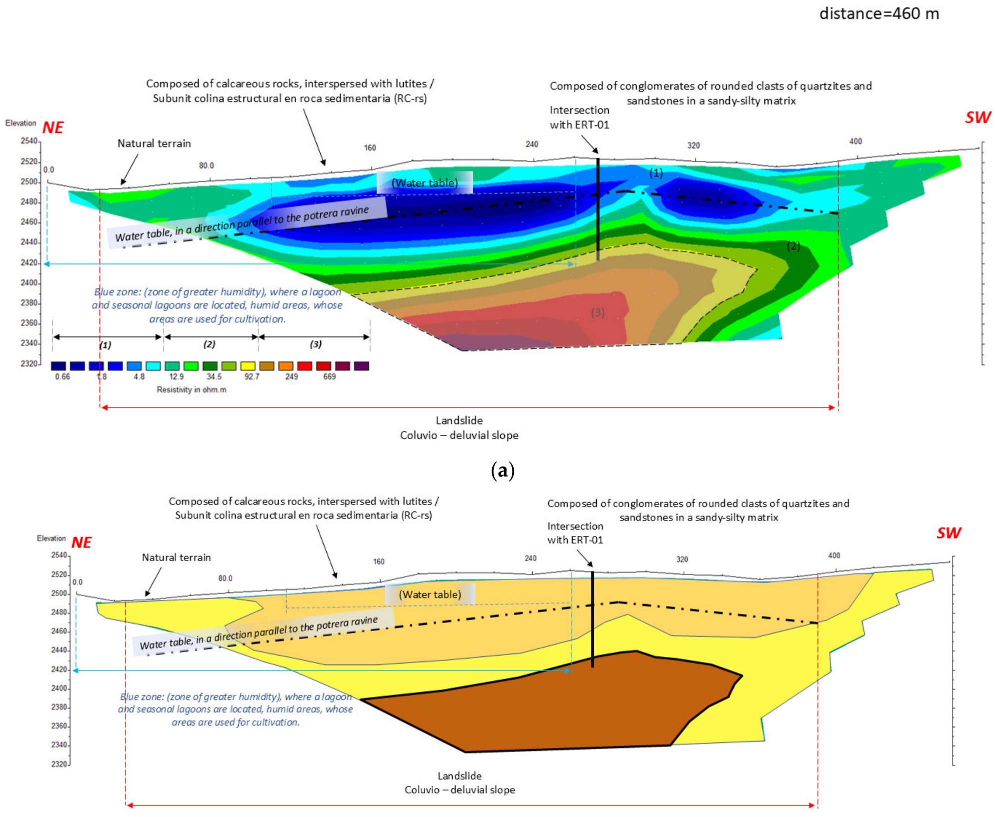

(**a**)

(**b**)

Figure 17. ERT-4 profile. (**a**) Interpreted profile with respect to the resistivities obtained in the field readings. (**b**) Stratigraphic profile.

There is an initial layer of low electrical resistivity, represented by a resistivity of between 0.6 and 8. 9 Ohm·m, made up of calcareous rocks, interspersed with shales with rounded, sub-rounded, and angular clasts of fossiliferous limestone and brown-yellowish marl with intercalated clays and small lithic fragments of sandstone, this being the stratum with the highest humidity and/or saturation. The second layer consists of calcareous sedimentary rock interbedded with shale, exhibiting low to moderately high moisture content and an average resistivity ranging from 8.9 to 92.7 Ohm·m. The third layer, with high resistivities ranging from 92.7 to 669 Ohm·m, consists of calcareous sedimentary rock interbedded with shale. It is a slightly moist stratum of unknown thickness. The depths of the materials and the resistivities characteristic of each stratum in each profile are variable (Table 3).

Table 3. Results of electrical tomography by stratum.

ERT	Estratum	Thickness (m)	Rho (Ohm·m)
ERT-1	1 *	25.0–75.0	0.6–8.8
	2 **	35.0–55.0	8.8–92.3
	3 ***	-	92.3–666
ERT-2	1 *	25.0–130.0	0.6–8.8
	2 **	45.0–110.0	8.8–92.5
	3 ***	-	92.5–667
ERT-3	1 *	10.0–90.0	0.6–8.8
	2 **	45.0–100.0	8.8–92.6
	3 ***	-	92.6–668
ERT-4	1 *	60.0–130.0	0.6–8.8
	2 **	45.0–100.0	8.8–92.7
	3 ***	-	92.7–669

* Material composed of calcareous rocks interbedded with shales, containing rounded, sub-rounded, and angular clasts of fossiliferous limestone and yellowish-brown marl with intercalated clays and small lithic fragments of sandstone. This stratum exhibits high moisture content and/or saturation. ** Material composed of calcareous sedimentary rock interbedded with shale, with low to slightly moist humidity. *** Material composed of calcareous sedimentary rock interbedded with shale, with low to slightly moist humidity.

The results indicate that via the structural behavior of the rocks in the four profiles and modeling of the subsoil, three variable thicknesses of strata can be distinguished, which reveal low and high resistivities (Figure 18). According to this research, the minimum is 0.6 Ohm·m and the maximum is 669 Ohm·m. According to [48], these soils are found in marl, clay, silt, limestone sand, and sandstone, as well as in the presence of fresh water.

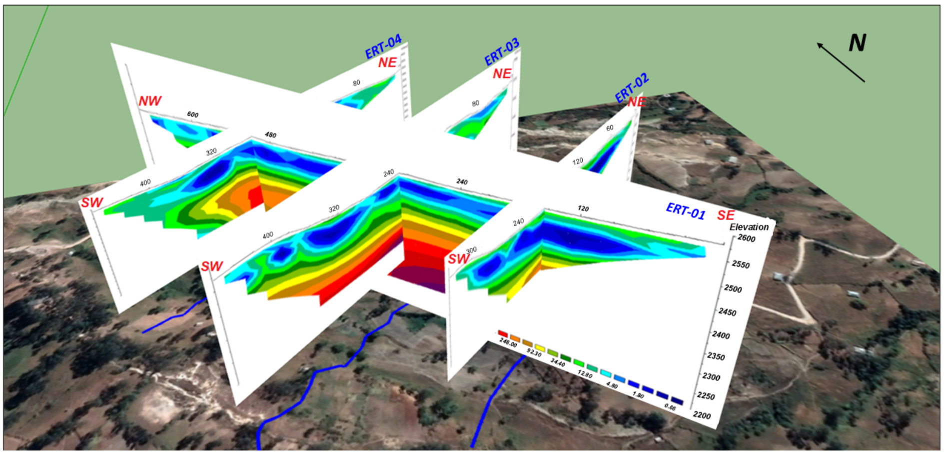

Figure 18. Combination of tomography lines in a pseudo 3D model.

In turn, in the study area, it is possible to identify the Hill unit, made up of the geomorphological sub-units Colluvial–Deluvial slope (V-cd), characterized by its gravose composition, boulders, and sandy matrices, both fine and coarse-grained, arranged in layers that are easy to disintegrate, with low compaction and high porosity; and the structural hill sub-unit in sedimentary rock (RC-rs), correlated with the Celendín formation, is made up of calcareous rocks interspersed with shales.

The predominant geological units in the area are quaternary deposits, tertiary volcanic rocks, and Paleozoic metamorphic rocks [29]. The age of most of the strata is classified as the Mesozoic of the Upper Cretaceous system. There are two stratigraphic units: the Chota and Celendín formations. The geomorphological characteristics and stratigraphic units present a large quantity of shale, limestone, and other components (Figure 7). Formations based on alternating shale and sandstone and weathered formations are prone to instability and are common in landslides [62]. Therefore, the influence of local formations is directly related to the mass movements in the province of Chota.

6. Discussion

The interdisciplinary research carried out in the area of the Laguna del Amor landslide has allowed for a comprehensive understanding of the geological, geomorphological, and hydrological factors involved in its stability. Using photogrammetry, the slopes, discontinuities, and the presence of scarps in the area were characterized. Likewise, the geological analysis allowed the determination of the composition of the soil, while the Electrical Resistivity Tomography (ERT) facilitated the identification of the underground flow of water, saturated strata, and the morphology of the landslide. This study is one of the first of its kind in this region, in the face of a scarcity of data, professionals, equipment, software and hardware, in an area of tourist interest for the development of the city of Chota [63], making research into the resistive properties of the stratigraphy of the area essential.

The vertical electrical tomography method in the pole–dipole arrangement proved to be effective for evaluating landslides [18], identifying, in this case, a landslide with a SE–NW direction, with a stratum of very low resistivity, in which there is a variable depth fault plane associated with saturated materials, predominantly belonging to the Colluvial–Deluvial slope subunit [23]. The geological composition includes shale and weathered limestone, which are known to increase the risk of landslides [45–50].

The soils on the slopes of the Laguna del Amor area are classified as CH, concluding that the lithology and the presence of springs and marshy areas cause the instability [24]; likewise, the geophysical studies correlate with the strata with higher humidity and/or saturation such that the resistivities vary from 0.6 to 8. 8 Ohm·m. In turn, it is concluded that a fundamental parameter for evaluating the prediction of landslides is the displacement of slopes due to the ease of data collection; likewise, the structural degradation of a slope has an influence on the freezing and thawing of the land [13–16].

The low resistivity of the materials indicates the existence of saturated or clayey materials, and the geology and geomorphology of the area indicate the existence of clayey formations and highly weathered sedimentary rocks (shale and limestone), while the climate (Figure 6) of the area suggests high saturation of the strata. Therefore, the existence of these two factors is what causes the landslide and the imminent risk in the sector. These are the main conditions for the activation of the landslide at present [4–64].

The electrical resistivity profiles revealed three distinct layers. The first layer, of low resistivity with a resistivity between 0.6 and 8.9 Ohm·m, is composed of calcareous rocks with intercalated shales and saturated soil. The second layer has resistivity values between 8.8 and 92.6 Ohm·m and corresponds to calcareous sedimentary rocks with intercalated shales and slight humidity. Finally, the third layer, with resistivities between 92.7 and 669 Ohm·m, is composed of calcareous materials with intercalated shales with lower moisture content. In the Lagunas sector, the existing materials are predominantly sedimentary. Throughout their stratigraphy, these strata are very common in landslides. Their behavior can be summarized as absorbing water and gradually losing their stability due to the swelling of the shales, tending to soften and disintegrate, weakening the structure of the stratum, and causing a landslide. This would explain why the fault plane occurs in the area of greatest saturation.

This is the case of the landslide in the lagoon sector due to the fact that it has been activated since the intercalations of materials present complex behaviors in the face of water saturation. This would explain why the stratum with the highest saturation is stratum number 1, as the shales would prevent water from infiltrating into lower strata unless they lost their consistency and shape, activating the landslide.

In shallower areas (less than 300 m depth), resistivities up to 400 Ohm·m suggest the presence of fault discontinuities or changes in rock composition [18]. Also, a resistivity range of 30–50 Ohm·m was observed in the first 6 m, indicating clays, whose influence persists down to a depth of 18 m [17]. In studies of gravity morphostructures, resistivities up to 15,600 Ohm·m indicate rock fracturing and the presence of moisture [65]. These findings are consistent with previous studies describing the sedimentary geology of the region and its predisposition to instability due to groundwater flow and high runoff [23–32].

Analysis of the geology of Laguna del Amor identified conglomerates with rounded clasts (5–20 cm diameter) supported by a sandy matrix and sandy-loamy strata of the Chota Formation, together with the underlying Celendín Formation. In-filtration points ("ojos de agua") and accumulations in slipped areas were detected, reflecting the constant interaction between groundwater and soil materials. The presence of steep slopes (up to 35°) and persistent water infiltration reduce the angle of internal friction and soil cohesion, exacerbating the risk of landslides.

The Laguna del Amor landslide is characterized as active, with slow movements in the direction of the lagoon. The morphological features observed, together with the results of the ERT, suggest a progressive movement with the potential for reactivation due to the persistence of weak materials in the underlying layers. This confirms the hazardous nature of the area, especially for dwellings located in vulnerable areas.

The combination of ERT, geology, and photogrammetry allowed for a detailed analysis of the triggering factors of the landslide. The lack of previous investigations in this region underlines the need for additional studies, such as Seismic Refraction, Multichannel Analysis of Surface Waves (MASW-MASW-2D), Multichannel Analysis of Microtremors (MAMs or REMI), and Time Domain Electromagnetic Methods (TDEMs) analyses and drilling, could make it interesting to corroborate and expand the findings. The results will provide a solid basis for future mitigation and planning interventions in Laguna del Amor.

In the case of rock falls, it depends a lot on the slope in the experimental analysis of the kinematics of rocks in the Tibet Autonomous Region. The angles of inclination are approximately 24°, 34°, and 52°. The block is cube-shaped, with a variable mass between 40.65 and 42.45 kg, and was thrown from a height of 4.5 m with a fall angle of 40°. Under these conditions, it reached a maximum average modified speed of 10.15 m/s. These results were obtained at maximum gradient. Furthermore, the improved discontinuous deformation analysis was used to simulate a rocky slope subjected to a wedge failure [14,15]. In the study area, Figure 2, it is mainly located on slopes of 0 to 15 (green), and it can be seen that there may be landslides and collapses to the southwest and northeast because the slopes are greater than 45 degrees (red).

7. Conclusions

The results of this research highlight the effectiveness of Electrical Resistivity Tomography in its pole–dipole configuration to characterize the landslide in the Laguna del Amor area, providing a detailed understanding of the geometry and structure of the affected terrain. The results obtained validate previous geological observations and identify areas of saturation, material disposition, and the constituent parts of the landslide, including the plane of failure and its internal limits. This demonstrates the potential of the geophysical method to complement and validate geological studies in high-risk areas.

The characterization of the subsoil, as shown in the modeling of the subsoil profiles, allowed the identification of three main layers: a saturated layer with low resistivities (0.6–8.8 Ohm·m), a layer with moderate to light moisture (8.8–93 Ohm·m), and a layer with low moisture (93–664 Ohm·m). These differences reflect the influence of saturation on the stability of the terrain, confirming the heterogeneity of the subsoil and its direct relationship with susceptibility to landslides.

When investigating landslides, photogrammetry is an essential and innovative tool for obtaining morphological data (obtaining DEM images in areas that are difficult to access and dangerous); in this investigation, it was possible to identify the slopes in the body of the landslide that are in the range of 0–15° (green). Around the scarps and at the foot of the sliding slope, there are slopes ranging from 15 to 25°. Likewise, the scarps (Figure 3) can be seen in orange with slopes between 25 and 45° within the area of the landslide marked in blue (Figure 2). Similarly, slopes greater than 45° are present to the southwest and northeast (red) of the study area (Figure 2).

The analysis of the heights shows five (5) sections every 34 m, defining the slopes and the direction of the avalanches, which go in the direction of the Potrera ravine at the foot of the landslide (Figure 4b,h). It is also inferred that the landslide is heading in an SE–NW direction, as evidenced by the body of the landslide (Figure 5).

In addition, the danger of slipping in the Laguna del Amor is confirmed. The current structural conditions of the terrain are marked by highly saturated materials, with a notable presence of sedimentary deposits (fragments of calcareous rocks and mudstones). The geological configuration (Celendín and Chota geological formation, as well as the presence of the geomorphological units of Colluvial–Deluvial slope and the subunit of structural hill in sedimentary rock). Furthermore, the unfavorable geomorphology indicates a significant risk of reactivation. This conclusion is consistent with previous studies in similar contexts, which highlight the need for continuous monitoring and mitigation measures.

Finally, the application of the pole–dipole array proved highly effective, showing an adequate resolution to identify discontinuities and variations in the subsoil. This positions Electrical Resistivity Tomography as an essential tool for the evaluation of landslides in areas of high geological complexity, such as the one studied. The findings presented constitute a solid basis for future studies and risk management actions in the region. The data obtained in this research, as well as the methodology and analysis of results, are applicable to any research or project correlated with slope stabilization, as well as in the characterization of the subsoil of any kind of project since the dipole–pole arrangement, with data inversion using RES2DINV v.3.53, has proven to have the capacity and detail for an analysis as complex as a landslide.

ERT 3D monitoring is recommended for its high precision in the evaluation of landslides and slopes [49–66] in order to determine local data on soil moisture in swampy areas or in the presence of bofedales, which are located mainly in the central part of the landslide, to implement mitigation actions, such as deep drainage to reduce saturation and improve natural drainage, and in order to stabilize the water table and partially restore soil cohesion in the most compromised areas.

Author Contributions: Conceptualization, A.Z., J.T., C.S., J.C. and P.C.; methodology A.Z., J.T., C.S., J.C. and P.C.; software, A.Z., J.T., C.S., J.C. and P.C.; validation, A.Z., J.T., C.S., J.C. and P.C.; formal analysis, A.Z., J.T., C.S., J.C. and P.C.; investigation, A.Z., J.T., C.S., J.C. and P.C.; resources, A.Z., J.T., C.S., J.C. and P.C.; data curation, A.Z., J.T., C.S., J.C. and P.C.; writing—original draft preparation, A.Z., J.T., C.S., J.C. and P.C.; writing—review and editing, A.Z., J.T., C.S., J.C. and P.C.; visualization, A.Z., J.T., C.S., J.C. and P.C.; supervision, P.C.; project administration, A.Z.; funding acquisition, A.Z. All authors have read and agreed to the published version of the manuscript.

Funding: This research received no external funding.

Data Availability Statement: The original contributions presented in this study are included in the article. Further inquiries can be directed to the corresponding author(s).

Acknowledgments: We would like to thank the company ZEAR ENGINEERING.SAC for processing the Electrical Resistivity Tomography studies and Livaque Constructores E.I.R.L. for processing the digital elevation models.

Conflicts of Interest: The authors declare that they have no conflicts of interest.

References

1. Vilchez, M. Casos Históricos de Movimientos en Masa que Causaron Grandes Daños en Perú. Instituto Geológico, Minero y Metalúrgico—INGEMMET [Internet]. 2018. Available online: https://repositorio.ingemmet.gob.pe/handle/20.500.12544/2590 (accessed on 28 October 2024).
2. Omowumi, F.; Kanungo, D.P.; Chauhan, P.K.S.; Dash, R. Recent Trends in Application of Electrical Resistivity Tomography for Landslide Study. *Renew. Energy Its Innov. Technol.* **2019**, *1*, 195–204. Available online: https://link.springer.com/chapter/10.1007/978-981-13-2116-0_16 (accessed on 30 October 2024).
3. Perrone, A.; Lapenna, V.; Piscitelli, S. Electrical resistivity tomography technique for landslide investigation: A review. *Earth Sci. Rev.* **2014**, *135*, 65–82. [CrossRef]
4. Cruden, D.M.; Varnes, D.J. *Landslide Types and Processes, Transportation Research Board*; Special Report; U.S. National Academy of Sciences: Washington, DC, USA, 1996; Volume 247, pp. 36–75. Available online: https://www.researchgate.net/publication/269710331_CrudenDMVarnes_DJ1996_Landslide_Types_and_Processes_Transportation_Research_Board_US_National_Academy_of_Sciences_Special_Report_247_36-75 (accessed on 9 February 2025).
5. Kamiński, M.; Zientara, P.; Krawczyk, M. Electrical resistivity tomography and digital aerial photogrammetry in the research of the "Bachledzki Hill" active landslide—In Podhale (Poland). *Eng. Geol.* **2021**, *285*, 106004. [CrossRef]
6. Crawford, M.; Bryson, L.S.; Woolery, E.; Wang, Z. Using 2-D electrical resistivity imaging for joint geophysical and geotechnical characterization of shallow landslides. *J. Appl. Geophy.* **2018**, *157*, 37–46. [CrossRef]
7. Batayneh, A.; Al-Diabat, A. Application of a two-dimensional electrical tomography technique for investigating landslides along the Amman-Dead Sea highway, Jordan. *Environ. Geol.* **2002**, *42*, 399–403. Available online: https://link.springer.com/article/10.1007/s00254-002-0543-x (accessed on 26 October 2024). [CrossRef]
8. Chalupa, V.; Pánek, T.; Tábořík, P.; Klimeš, J.; Hartvich, F.; Grygar, R. Deep-seated gravitational slope deformations controlled by the structure of flysch nappe outliers: Insights from large-scale electrical resistivity tomography survey and LiDAR mapping. *Geomorphology* **2018**, *321*, 174–187. [CrossRef]
9. Coşkun, N.; Çakır, Ö.; Erduran, M.; Kutlu, Y.A.; Çetiner, Z.S. A potential landslide area investigated by 2.5D electrical resistivity tomography: Case study from Çanakkale, Turkey. *Arab. J. Geosci.* **2016**, *9*, 1–20. Available online: https://link.springer.com/article/10.1007/s12517-015-2026-x (accessed on 26 October 2024). [CrossRef]
10. McCann, D.M.; Forster, A. Reconnaissance geophysical methods in landslide investigations. *Eng. Geol.* **1990**, *29*, 59–78. [CrossRef]
11. Corona, R. Tomografía de Resistividad Eléctrica (TRE) 2D para el Proyecto HAWC. Universidad Nacional Autónoma de México: México. 2014. Available online: https://repositorio.unam.mx/contenidos/tomografia-de-resistividad-electrica-tre-2d-para-el-proyecto-hawc-204380?c=BZ0EVn&d=false&q=*:*&i=1&v=1&t=search_0&as=0 (accessed on 31 October 2024).
12. Suhendra, S.; Elfrita, J.; Ikhlas, D.; Halauddin, H.; Supiyati, S. 2D and 3D Modelling Electrical Resistivity Tomography (ERT) of Landslide Sliding and Weak Bedding Plane Along Mountain Road North Bengkulu-Lebong, Indonesia. *Geosfera Indones.* **2024**, *9*, 29–40. Available online: https://jurnal.unej.ac.id/index.php/GEOSI/article/view/38065 (accessed on 8 February 2025). [CrossRef]
13. Liu, Y.; Cheng, P.; Liu, E.; Hu, J.; Cheng, Y.; Su, L. Seismic Response and Dynamic Failure Mode of a Class of Bedding Rock Slope Subjected to Freeze–Thaw Cycles. *Rock Mech. Rock Eng.* **2024**, 1–19. Available online: https://link.springer.com/article/10.1007/s00603-024-04318-2 (accessed on 2 February 2025). [CrossRef]
14. Liu, G.; Meng, H.; Song, G.; Bo, W.; Zhao, P.; Ning, B.; Xu, X. Numerical simulation of wedge failure of rock slopes using three-dimensional discontinuous deformation analysis. *Environ. Earth Sci.* **2024**, *83*, 1–31. Available online: https://link.springer.com/article/10.1007/s12665-024-11619-w (accessed on 2 February 2025). [CrossRef]
15. Liu, G.; Zhong, Z.; Ma, K.; Bo, W.; Zhao, P.; Li, Y.; Zhang, Z.; Zhang, P. Field experimental verifications of 3D DDA and its applications to kinematic evolutions of rockfalls. *Int. J. Rock Mech. Min. Sci.* **2024**, *175*, 105687. [CrossRef]
16. Zhang, X.; Luo, W.; Liu, G.; Yu, B.; Bo, W.; Zhao, P. An improved radial basis function neural network for displacement prediction of a reservoir slope. *Front. Earth Sci.* **2024**, *12*, 1389161. Available online: https://www.frontiersin.org/journals/earth-science/articles/10.3389/feart.2024.1389161/full (accessed on 2 February 2025). [CrossRef]
17. Agrahari, S.; Singh, A.; Yadav, A. Identification and estimation of the subsurface anisotropy from the 2D electrical resistivity tomography surveys. *J. Appl. Geophy.* **2024**, *230*, 105505. [CrossRef]

18. Porras, D.; Carrasco, J.; Carrasco, P.; González, P.J. Imaging extensional fault systems using deep electrical resistivity tomography: A case study of the Baza fault, Betic Cordillera, Spain. *J. Appl. Geophy.* **2022**, *202*, 104673. [CrossRef]
19. Zhu, T.; Zhou, J.; Wang, H. Localization and characterization of the Zhangdian-Renhe fault zone in Zibo city, Shandong province, China, using electrical resistivity tomography (ERT). *J. Appl. Geophy.* **2017**, *136*, 343–352. [CrossRef]
20. Funk, B.; Flores-Orozco, A.; Steiner, M. Possibilities and limitations of cave detection with ERT. *Geomorphology* **2024**, *462*, 109332. [CrossRef]
21. Marín, K.; Sangay, J. Estudio hidrogeológico mediante tomografía geoeléctrica para la localización de aguas subterráneas en el centro poblado La Huaraclla—Jesús—Cajamarca 2020. [Tesis para optar el título profesional de: Ingeniero Geológico]. Universidad Privada del Norte. Universidad Privada del Norte. 2021. Available online: https://repositorio.upn.edu.pe/handle/11537/24979 (accessed on 27 October 2024).
22. Huanca, R. Tomografía electrica para el mantenimiento de la carretera longitudinal tramo II—La Libertad [Arequipa]: Universidad Nacional de San Agustin de Arequipa; 2019. Available online: http://repositorio.unsa.edu.pe/handle/UNSA/10765 (accessed on 27 October 2024).
23. León, L.; Zavaleta, A. Repositorio Institucional INGEMMET. Instituto Geológico, Minero y Metalúrgico—INGEMMET; 2022. Evaluación del deslizamiento rotacional en el sector Lagunas, distrito Chota, provincia Chota, departamento Cajamarca. Available online: https://repositorio.ingemmet.gob.pe/handle/20.500.12544/3618 (accessed on 27 October 2024).
24. Barboza, A. Factor de seguridad en las laderas del sector Las Lagunas—Chota—Cajamarca con métodos geotécnicos y Software Slide. Universidad Nacional de Cajamarca. 2024. Available online: http://repositorio.unc.edu.pe/handle/20.500.14074/7460 (accessed on 2 February 2025).
25. Suski, B.; Brocard, G.; Authemayou, C.; Consenza, M.B.; Teyssier, C.; Holliger, K. Localization and characterization of an active fault in an urbanized area in central Guatemala by means of geoelectrical imaging. *Tectonophysics* **2010**, *480*, 88–98. [CrossRef]
26. Sáez, C.; Martín, I.; Maté, M.; Carrasco, P.; Farfán, M.; González-Aguilera, D. Geophysical exploration for shallow geothermal applications: A case study in Artà, (Balearic Islands, Spain). *Geothermics* **2022**, *105*, 102517.
27. Phan, N.; Leung, A.; Nguyen, T.; Kamchoom, V.; Likitlersuang, S. Modelling root decomposition effects on root reinforcement and slope stability. *Comput. Geotech.* **2025**, *179*, 107024. [CrossRef]
28. Li, Y.; Yang, G.; Lin, Y.; Zhao, T.; Duan, R.; Li, H. Research on the shallow landslide stability of vegetated slopes with expansive soils based on root morphology. *Ecol. Model.* **2024**, *496*, 110808. [CrossRef]
29. Boulangger, R.E.; Sipión, B.C.D. Estudio de recursos de rocas y minerales industriales para la inclusión económica social y desarrollo en la región Cajamarca—[Boletín B 68] [Internet]. Instituto Geológico, Minero y Metalúrgico—INGEMMET. Lima: Instituto Geológico, Minero y Metalúrgico—INGEMMET. 2020. Available online: https://repositorio.ingemmet.gob.pe/handle/20.500.12544/2800 (accessed on 28 October 2024).
30. Wilson, J. *Geología de los cuadrángulos: Jayanca (13-d), Incahuasi (13-e), Cutervo (13-f), Chiclayo (14-d), Chongoyape (14-e), Chota (14-f), Celendin (14-g), Pacasmayo (15-d) y Chepen (15-e)*; Instituto Geológico Minero y Metalúrgico: Perú, Lima, 1984.
31. Servicio Nacional de Meteorología e Hidrología del Perú. SENAMHI. 2024. Available online: https://www.senamhi.gob.pe/?p=pronostico-meteorologico (accessed on 2 February 2025).
32. Tapia, H. Evaluación de riesgo por fenómeno de remoción en masas en la comunidad de Santa Rosa, provincia de Chota—Cajamarca [Internet]. Universidad nacional de Cajamarca: Cajamarca. 2024. Available online: http://repositorio.unc.edu.pe/handle/20.500.14074/6957 (accessed on 31 October 2024).
33. Instituto Geológico Minero y Metalúrgico. INGEMMET. 2024. Available online: https://portal.ingemmet.gob.pe/web/guest/presentacion (accessed on 2 February 2025).
34. Sistema de Información Geológico y Catastral Minero. GEOCATMIN. 2024. Available online: https://geocatmin.ingemmet.gob.pe/geocatmin/ (accessed on 5 February 2025).
35. Bestyński, Z.; Pacanowski, G.; Sieinski, E. Badania geofizyczne i klasyfikacje geotechniczne w ocenie stateczności karpackich zboczy fliszowych. *Przegląd Geol.* **2017**, *65*, 717–724. Available online: https://geojournals.pgi.gov.pl/pg/article/view/27168 (accessed on 23 October 2024).
36. Bestyński, Z.; Thiel, K. Geophysical investigations of the Carpathian slide slopes. *Pol. Geol. Inst. Spec. Pap.* **2005**, *20*, 35–39.
37. Calamita, G.; Gallipoli, M.R.; Gueguen, E.; Sinisi, R.; Summa, V.; Vignola, L.; Stabile, T.A.; Bellanova, J.; Piscitelli, S.; Perrone, A. Integrated geophysical and geological surveys reveal new details of the large Montescaglioso (southern Italy) landslide of December 2013. *Eng Geol.* **2023**, *313*, 106984. [CrossRef]
38. Travelletti, J.; Malet, J.P.; Samyn, K.; Grandjean, G.; Jaboyedoff, M. Control of landslide retrogression by discontinuities: Evidence by the integration of airborne- and ground-based geophysical information. *Landslides* **2013**, *10*, 37–54. Available online: https://link.springer.com/article/10.1007/s10346-011-0310-8 (accessed on 28 October 2024). [CrossRef]
39. Marciniak, A.; Kowalczyk, S.; Gontar, T.; Owoc, B.; Nawrot, A.; Luks, B.; Cader, J.; Majdański, M. Integrated geophysical imaging of a mountain landslide—A case study from the Outer Carpathians, Poland. *J. Appl. Geophy.* **2021**, *191*, 104364. [CrossRef]

40. Luhn, J.; Stumvoll-Schmaltz, M.; Flores, A.; Glade, T. Internal structure of an active landslide based on ERT and DP data: New insights from the Hofermühle landslide observatory in Lower Austria. *Geomorphology* **2023**, *441*, 108910. [CrossRef]
41. Flores, A.O.; Steiner, M.; Katona, T.; Roser, N.; Moser, C.; Stumvoll, M.J.; Glade, T. Application of induced polarization imaging across different scales to understand surface and groundwater flow at the Hofermuehle landslide. *Catena* **2022**, *219*, 106612. [CrossRef]
42. Binley, A.; Kemna, A. DC Resistivity and Induced Polarization Methods. *Hydrogeophysics* **2005**, 129–156. Available online: https://link.springer.com/chapter/10.1007/1-4020-3102-5_5 (accessed on 6 February 2025).
43. Pasierb, B. The application of the 2D/3D electrical resistivity tomography (ERT) method in investigating the carbonate karst of the Zakrzówek Horst. *Geol. Geophys. Environ.* **2022**, *48*, 319–327. Available online: https://journals.agh.edu.pl/geol/article/view/4830 (accessed on 21 October 2024). [CrossRef]
44. Edwards, L.S. A modified pseudosection for resistivity and IP. *Geophysics* **1977**, *42*, 1020–1036. [CrossRef]
45. Loke, M.H. Electrical imaging surveys for environmental and engineering studies. pages.mtu.eduMH LokeA practical guide to, 1999•pages.mtu.edu [Internet]. 2000. Available online: https://pages.mtu.edu/~ctyoung/LOKENOTE.PDF (accessed on 21 October 2024).
46. Dahlin, T.; Zhou, B. A numerical comparison of 2D resistivity imaging with 10 electrode arrays. *Geophys. Prospect.* **2004**, *52*, 379–398. [CrossRef]
47. Bellanova, J.; Calamita, G.; Giocoli, A.; Luongo, R.; Macchiato, M.; Perrone, A.; Uhlemann, S.; Piscitelli, S. Electrical resistivity imaging for the characterization of the Montaguto landslide (southern Italy). *Eng. Geol.* **2018**, *243*, 272–281. [CrossRef]
48. Orellana, E. *Prospección Geoeléctrica en Corriente Continua*; Paraninfo: Madrid, Spain, 1972.
49. Fäth, J.; Kneisel, C. Combined 2D- and 3D ERT monitoring as a geophysical tool for investigating spatial and temporal soil moisture fluctuations in a pine-beech forest. *Trees For. People* **2024**, *16*, 100555. [CrossRef]
50. Chambers, J.E.; Wilkinson, P.B.; Kuras, O.; Ford, J.R.; Gunn, D.A.; Meldrum, P.I.; Pennington, C.V.; Weller, A.L.; Hobbs, P.R.; Ogilvy, R.D. Three-dimensional geophysical anatomy of an active landslide in Lias Group mudrocks, Cleveland Basin, UK. *Geomorphology* **2011**, *125*, 472–484. [CrossRef]
51. Martorana, R.; Capizzi, P.; D'Alessandro, A.; Luzio, D. Comparison of different sets of array configurations for multichannel 2D ERT acquisition. *J. Appl. Geophy.* **2017**, *137*, 34–48. [CrossRef]
52. Jongmans, D.; Garambois, S. Geophysical investigation of landslides: A review. *Bull. Société Géologique Fr.* **2007**, *178*, 101–112. [CrossRef]
53. Morelli, S.; Utili, S.; Pazzi, V.; Castellanza, R.; Fan, X. Landslides and Geophysical Investigations: Advantages and Limitations. *Int. J. Geophys.* **2019**, *2019*, 8732830. [CrossRef]
54. Sasaki, Y. Resolution of resistivity tomography inferred from numerical simulation. *Geophys. Prospect.* **1992**, *40*, 453–463. [CrossRef]
55. deGroot-Hedlin, C.; Constable, S. Occam's inversion to generate smooth, two-dimensional models from magnetotelluric data. *Geophysics* **1990**, *55*, 1613–1624. [CrossRef]
56. Loke, M.H.; Barker, R.D. Rapid least-squares inversion of apparent resistivity pseudosections by a quasi-Newton method1. *Geophys. Prospect.* **1996**, *44*, 131–152. [CrossRef]
57. Olayinka, A.I.; Yaramanci, U. Use of block inversion in the 2-D interpretation of apparent resistivity data and its comparison with smooth inversion. *J. Appl. Geophy.* **2000**, *45*, 63–81. [CrossRef]
58. Dey, A.; Morrison, H.F. Resistivity modelling for arbitrarily shaped two-dimensional structures. *Geophys. Prospect.* **1979**, *27*, 106–136. [CrossRef]
59. de Bari, C.; Lapenna, V.; Perrone, A.; Puglisi, C.; Sdao, F. Digital photogrammetric analysis and electrical resistivity tomography for investigating the Picerno landslide (Basilicata region, southern Italy). *Geomorphology* **2011**, *133*, 34–46. [CrossRef]
60. Morelli, S.; Pazzi, V.; Frodella, W.; Fanti, R. Kinematic Reconstruction of a Deep-Seated Gravitational Slope Deformation by Geomorphic Analyses. *Geosciences* **2018**, *8*, 26. [CrossRef]
61. Idrogo, J.; Sagástegui, G. Accuracy of the digital terrain model (DTM), considering the number of ground support points in a photogrammetric survey applied on the Pampa Grande-Tablazos highway, Chiclayo Province. *ALICIA*. 2022. Available online: https://research.upn.edu.pe/en/publications/precisi%C3%B3n-del-modelo-digital-de-terreno-mdt-considerando-el-n%C3%BAmer/fingerprints/ (accessed on 29 October 2024).
62. Picarelli, L.; di Maio, C. Deterioration processes of hard clays and clay shales. *Geol. Soc. Eng. Geol. Spec. Publ.* **2010**, *23*, 15–32. Available online: https://pubs.geoscienceworld.org/gsl/books/edited-volume/1520/chapter/107204872/Deterioration-processes-of-hard-clays-and-clay (accessed on 24 October 2024). [CrossRef]
63. Escobar, E. Ministerio de Comercio Exterior y Turismo [MINCETUR] [Internet]. 2022. Available online: https://consultasenlinea.mincetur.gob.pe/fichaInventario/index.aspx?cod_Ficha=11326 (accessed on 2 February 2025).
64. Highland, L.; Bobrowsky, P. The Landslide Handbook-A Guide to Understanding Landslides. USGS: Virginia [Internet]. 2008. Available online: https://pubs.usgs.gov/circ/1325/pdf/C1325_508.pdf (accessed on 23 March 2024).

65. Forno, M.G.; Gattiglio, M.; Gianotti, F.; Comina, C.; Vergnano, A.; Dolce, S. Deep Electrical Resistivity Tomography for Detecting Gravitational Morpho-Structures in the Becca France Area (Aosta Valley, NW Italy). *GeoHazards* **2024**, *5*, 886–916. [CrossRef]
66. Jia, N. Structural detection of goaf based on three-dimensional ERT technology. *Syst. Soft Comput.* **2025**, *7*, 200179. [CrossRef]